



Full Length Article

Average molecular structure model of shale kerogen: Experimental characterization, structural reconstruction, and pyrolysis analysis

Kanyuan Shi^{a,b,1}, Junqing Chen^{a,c,d,1,*}, Xiongqi Pang^{a,b,*}, Fujie Jiang^{a,b}, Shasha Hui^{a,b}, Sijia Zhang^{a,b}, Hong Pang^{a,b}, Yuying Wang^{c,d}, Di Chen^{a,b}, Xiaobin Yang^{c,d}, Bingyao Li^{c,d}, Tingyu Pu^{a,b}

^a State Key Laboratory of Petroleum Resources and Prospecting, China University of Petroleum, Beijing, Beijing 102249, China

^b College of Geosciences, China University of Petroleum, Beijing, Beijing 102249, China

^c Basic Research Center for Energy Interdisciplinary, College of Science, China University of Petroleum, Beijing, Beijing 102249, China

^d Beijing Key Laboratory of Optical Detection Technology for Oil and Gas, College of Science, China University of Petroleum, Beijing, Beijing 102249, China

ARTICLE INFO

Keywords:

Shale
Kerogen
Molecular dynamic simulation
ReaxFF molecular dynamic simulation
Nanpu Sag
Average molecular structure model

ABSTRACT

Shale can be both a source rock and a reservoir rock, which is a typical self-generating and self-storing type of oil accumulation. Its main organic component is kerogen. Using molecular dynamics (MD), a realistic kerogen molecular structure model is an alternative to experimental and analytical-only approaches for studying shale organic matter's microscopic properties. Therefore, it is useful to establish an average molecular structure model for shale kerogen. Moreover, the pyrolysis mechanism of shale kerogen is of great significance for developing and utilizing shale mineral resources. In this study, geochemical and spectroscopic measurements such as the elemental analysis, ¹³C nuclear magnetic resonance spectroscopy (¹³C NMR), Fourier transform infrared spectroscopy (FTIR), and X-ray photoelectron spectroscopy (XPS) were used to obtain information about the carbon skeleton, aliphatic structures, and aromatic structures of the kerogen. Following information analysis and molecular fragment splicing, a 2D molecular structure model of kerogen from the Nanpu shale, with the chemical formula C₁₉₉H₂₄₀O₂₀N₆S₂ and molecular weight of 3096 Daltons was constructed. After that, the accuracy of the 2D structure was verified by comparing the ¹³C NMR spectra simulated by the 2D structure to the experimental spectra. Using MD simulation, based on the kerogen density, 10 2D structures are then combined to create a realistic 3D molecular structure model of kerogen. Finally, pyrolysis analysis was performed based on the established 3D molecular structure model of kerogen to determine the effect of temperature on pyrolysis. Using the advantages of various technologies, this study not only provides a systematic method for establishing a realistic 3D molecular structure model of kerogen but also contributes to in-depth research on the reaction mechanism of kerogen pyrolysis, providing a reliable foundation for future research on the properties of shale at the molecular scale.

1. Introduction

Shales can not only store but also produce oil and gas. It is a valuable fossil resource [1]. Shale oil is the accumulation of oil in shale formations rich in organic matter and dominated by nanoscale pore sizes. It is an important alternative energy source for oil and gas in the future and is of great significance for alleviating energy crises and promoting sustainable economic development [2,3,4]. Shale gas is abundant in resources, easy to store and transport, and relatively environmentally

friendly when compared to other resources like coal. It is a significant replacement resource for conventional oil and gas supplies [5]. According to the Energy Information Administration (EIA) energy outlook, the global recoverable capacity of shale oil technology is 345 billion barrels [6]. Shale gas production will account for over 75% of total natural gas production in the coming decades [7]. Therefore, understanding the various properties of shale is beneficial to learning the characteristics of shale oil and gas reservoirs, thereby enhancing shale oil and gas recovery efficiency.

* Corresponding authors at: State Key Laboratory of Petroleum Resources and Prospecting, China University of Petroleum, Beijing, Beijing 102249, China.
E-mail addresses: cjq7745@163.com (J. Chen), pangxq@cup.edu.cn (X. Pang).

¹ These authors contributed equally to this work.

MD is currently an essential means of studying the microscopic behaviour of minerals [8]. MD methods have substantially expanded their theory, technology, and application domains since their inception and can now be applied to equilibrium and non-equilibrium systems [9]. MD simulation is a method that takes molecules as the primary research object, treats a system as a collection of molecules with specific characteristics, and uses classical mechanical methods to obtain the macroscopic characteristics by studying the microscopic molecules [10,11]. Due to its ability to simulate interactions between substances and accurately replicate experimental results, this method has been widely applied in fields such as materials, physical chemistry, and life sciences, as well as in the fields of geoscience and petroleum engineering [12]. Currently, many scholars have used molecular dynamics to study the adsorption, wetting angle changes, and mechanical properties on the surface of shale [13,14,15,16,17]. However, many scholars are currently using graphene to replace organic matter (mainly kerogen) in shale for research purposes [10,18,19,20,21]. Unlike the organic matter in shale, graphene has a TOC content of 100% and is entirely composed of carbon atoms. Thus, there may be some errors in the experimental results obtained [22]. Since a realistic molecular structure model of kerogen is the basis for studying the microscopic properties of shale organic matter using MD, it is necessary to establish a molecular structure model of shale kerogen for MD simulation research.

The molecular structure model of kerogen from oil shale and coal has been the subject of numerous investigations. For instance, Behar et al. (1987) analyzed the functional groups and pyrolysis properties of three different kerogen types from the United States Green River, France Toarcian, and Cameroon Douala using elemental analysis, electron microscopy, ^{13}C NMR, and other techniques [23]. Through the statistical analysis, 2D molecular models of different types of oil shale kerogen were constructed. Siskin et al. (1995) obtained the carbon skeleton structure of kerogen by analyzing solid ^{13}C NMR data and used gas chromatography to statistically process the small molecules after the pyrolysis of kerogen [24]. Finally, a 2D molecular model of kerogen with the molecular formula $\text{C}_{645}\text{H}_{1017}\text{N}_{19}\text{O}_{17}\text{S}_4$ was constructed. It should be noted that kerogen is the organic matter in sedimentary rocks that is not extractable by organic solvents and is a product of diagenesis. Every kerogen is a little different (or a lot different), based on source materials, preservation during deposition, and its diagenetic history. Ru et al. (2012) used elemental analysis, ^{13}C NMR, FTIR, and other testing methods to analyze the molecular structure of the kerogen statistically [25]. They constructed a 2D molecular model of kerogen with the chemical formula $\text{C}_{243}\text{H}_{407}\text{O}_3\text{N}_{25}\text{S}_2$. Computer quantum chemistry and MD methods were used to optimize the 2D structure model of kerogen to obtain the 3D molecular model. Wang et al. (2015) and Guan et al. (2015) conducted XRD, ^{13}C NMR, FTIR, and XPS experiments on five different types of oil shale kerogens (Huadian, Jilin, Yaojie, Gansu, Longkou, Fushun, Liaoning, and Maoming, Guangdong) [26,27]. Taking Huadian oil shale kerogens in China as an example, a set of carbon skeleton isomers of Huadian oil shale kerogens was constructed, and computer quantum chemical calculation methods were used. The stability of isomer models with various carbon skeletons resulting from various substitutional positions of functional groups was discussed, and a relatively stable 3D molecular structure model of kerogen in the isomers was summarized. Liu et al. (2021) used ^{13}C NMR, FTIR, XPS, high-resolution transmission electron microscopy (HRTEM), and elemental analyses to construct the 2D molecular structure of kerogen. Comparative experiments and calculated ^{13}C NMR spectra verified the connection of kerogen fragments [28]. The final 3D model's density and micropore structure were verified using experimental helium density and micropore volume. It can be seen that there have been previous studies on the molecular structure modeling of kerogen. However, there is relatively little research on utilizing multiple experimental methods to construct kerogen models and providing detailed descriptions of the modeling process for kerogen. Moreover, no one has constructed the average molecular structure of kerogen in Nanpu shale. Therefore, it is

necessary to build an average molecular structure model of shale (taking Nanpu shale as an example) kerogen. "Average molecular structure" refers to an atomic aggregate after averaging the number of aromatic clusters in the structure. It cannot be regarded as the chemical structure of any specific molecule in the group, but as a mathematical model, which can reflect the typical chemical and physical properties of the mixture molecular group [29]. Because of the complex composition and structure of kerogen, it is extremely difficult to get the molecular structure model to reach the level of simulation. The analysis data based on which the model is designed cannot be comprehensive. The molecular structure model designed should be an expression of the average molecule of kerogen, which does not mean that the assumption of the actual molecular size of kerogen is given. This concept has been widely used in the study of the chemical structure of coal, kerogen, and various asphalts [25,30,31]. In fact, kerogen is usually chemically reacted by molecular group, so it is feasible and reasonable to use "average molecular structure" to describe kerogen.

The pyrolysis of kerogen is a very complex process [32]. At present, thermogravimetry-mass spectrometry, microwave pyrolysis technology, and thermal simulation of hydrocarbon generation are mostly used to analyze pyrolysis products. However, using experimental methods can only achieve macroscopic analysis of pyrolysis products; They cannot collect microscopic details and reveal the pyrolysis mechanism [33]. The Reax FF MD combines the advantages of Quantum chemistry and traditional MD methods, and can be used to simulate the chemical reaction process of complex systems without preset reaction paths, which makes it possible to study the pyrolysis mechanism at the molecular level [34]. ReaxFF MD has many advantages and potential in studying complex systems involving chemical reactions, including its ability to handle large systems with thousands of atoms and dynamic optimization of atomic charges [35]. ReaxFF MD simulation methods can shorten research time, reduce research consumption, and achieve microscopic descriptions of the dynamic process of chemical reactions. Simultaneously, quantum chemistry calculations have substantially improved, making it possible to examine intricate reaction pathways of numerous chemicals [36]. Salmon et al. (2009) used ReaxFF MD to simulate the decomposition and formation of functional groups in the pyrolysis process of Morwell lignite [37]. Zhang et al. (2014) explored the thermal decomposition mechanism of Hatcher sub-bituminous coal using the same method [38]. According to the calculation results, the pyrolysis reaction of Hatcher coal primarily starts with intramolecular modifications, and the creation mechanisms of certain typical pyrolysis products are addressed Li et al. (2015) conducted a ReaxFF MD simulation at 1500 K to elaborate the formation path of CO_2 , H_2 , CH_4 and other pyrolysis gas product molecules [39]. Hong and Guo (2017) combined pyrolysis experiments with classical model pyrolysis simulation to study the effects of different temperatures and heating rates on the pyrolysis behavior of Zhundong coal, revealing the mechanism of tar secondary cracking [40]. Currently, research into coal pyrolysis is the main emphasis of ReaxFF MD modeling techniques. ReaxFF MD simulation techniques, however, have many benefits and can potentially be used in the analysis of intricate and large-scale systems involving chemical reactions and will also be widely used in pyrolysis and combustion of shale kerogen.

In this study, the shale in the Nanpu area was selected as the actual sample. Firstly, a 2D molecular structure model of kerogen in this area was constructed using elemental analysis, ^{13}C NMR, FTIR, and XPS experiments. Secondly, the accuracy of the 2D structure is verified by comparing the ^{13}C NMR spectra simulated by the 2D structure with the experimental spectra. Next, a realistic 3D molecular structure model of kerogen is established using MD simulation based on kerogen density. Finally, based on the established 3D molecular structure model, pyrolysis analysis was conducted to determine the effects of pyrolysis temperature on pyrolysis. Using the advantages of various technologies, this study not only provides a systematic method for establishing a realistic 3D molecular structure model of kerogen, but also can characterize the

kinetics of microscopic reactions on an atomic scale, contributing to the in-depth study of the reaction mechanism of kerogen pyrolysis.

2. Samples and methods

2.1. Preparation of shale samples and kerogen

A shale (Lacustrine shale) sample was used from the Gaoshangbao region (Fig. 1a and b), located northeast of Nanpu Sag in the Bohai Bay Basin, China. There are two main reasons for choosing which shale

sample to extract kerogen from. (1) In order to make our extraction of kerogen more effective, we need to choose samples with high TOC content. (2) In order to comprehensively characterize the changes in the characteristics of hydrocarbon generation products in kerogen samples, it is necessary to use low maturity samples for pyrolysis analysis. This area is a long-established anticlinal structural belt dominated by NW and NE trending faults and one of Nanpu Sag's primary onshore oil-producing regions [41]. The Bohai Bay Basin is one of the most important hydrocarbon generating regions in China. The sample is grayish black, with a depth of 4108.9 m, and belongs to the Es₃ member

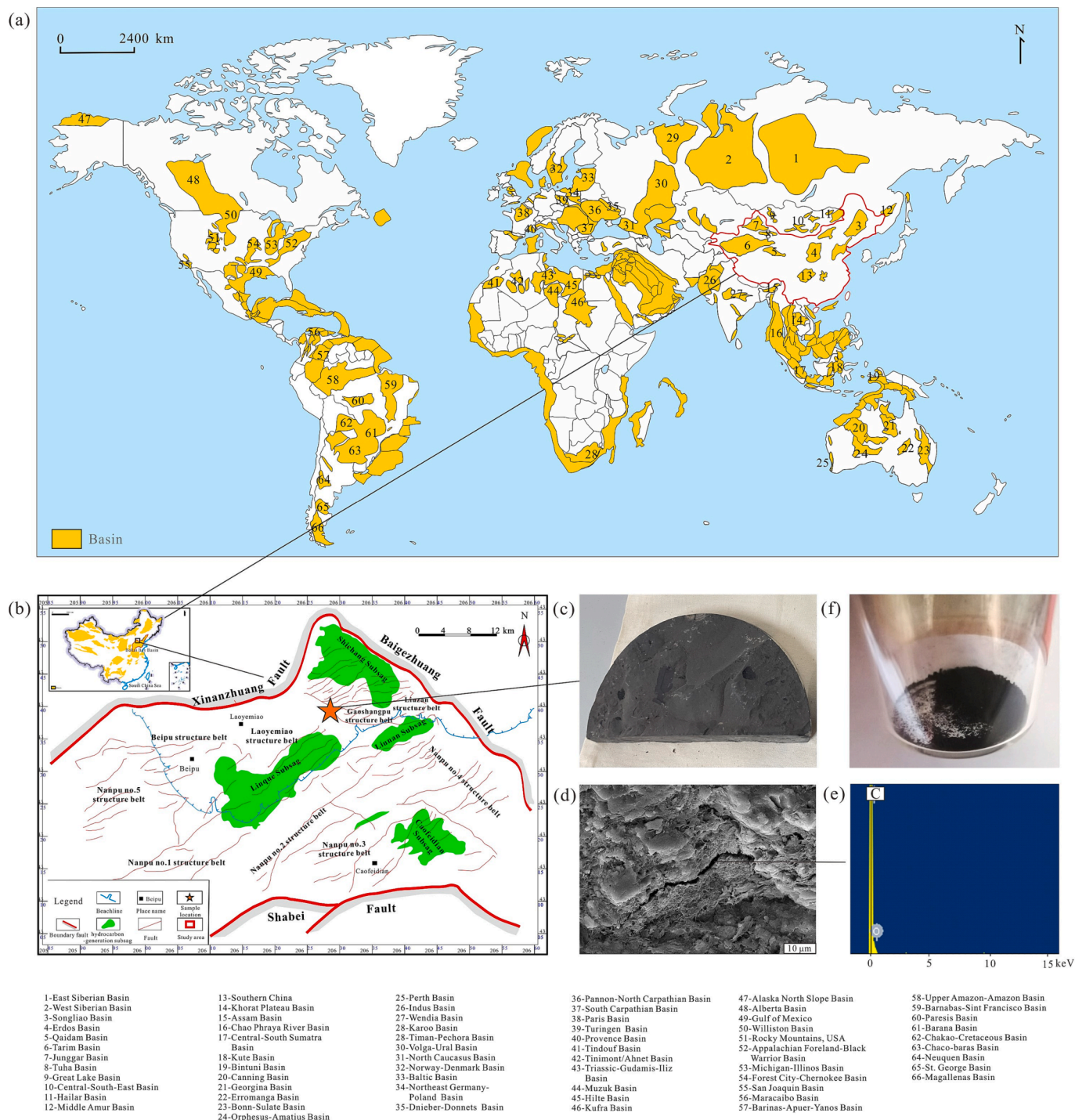


Fig. 1. (a) Distribution of shale oil and gas-bearing basins worldwide (modified after [43]); (b) The geographical location of the shale sample; (c) Pictures of shale samples; (d) Field emission scanning electron microscope images of shale samples; (e) Prepared kerogen powder; (f) Energy spectrum images of organic matter in shale samples.

(Fig. 1c). Through the vitrinite reflectance measurement experiment, the Ro of shale sample is 0.63%, which is in the mature stage. Using the H/C and O/C atomic ratios of kerogen, it was determined that the shale sample is type II kerogen. The TOC content of this sample is 2.15%. Shale samples underwent field emission scanning electron microscopy, which revealed a dark, central stripe (Fig. 1d). The energy spectrum of the stripe revealed that the primary element was C, which is indicative of organic matter (Fig. 1e).

Before establishing the molecular structure of kerogen, it is first necessary to extract the kerogen from the shale. The extracted kerogen is

shown in Fig. 1f. The detailed process of kerogen extraction mainly involves five main steps, including acid treatment, alkali treatment, pyrite removal, heavy liquid separation, and chloroform asphalt cleaning of soluble organic matter (Fig. 2), meeting the GB/T 19144–2010 standard. Five acid treatments were performed to remove the main minerals from the matrix. HCl is used to dissolve carbonate minerals, while HCl and HF are used to dissolve quartz, clay minerals, and feldspar. Pyrite is removed by repeatedly mixing 6 mol/L of hydrochloric acid and arsenic-free zinc particles into the enriched sample and then washing it with distilled water until the reaction gas has no hydrogen sulfide odor. The

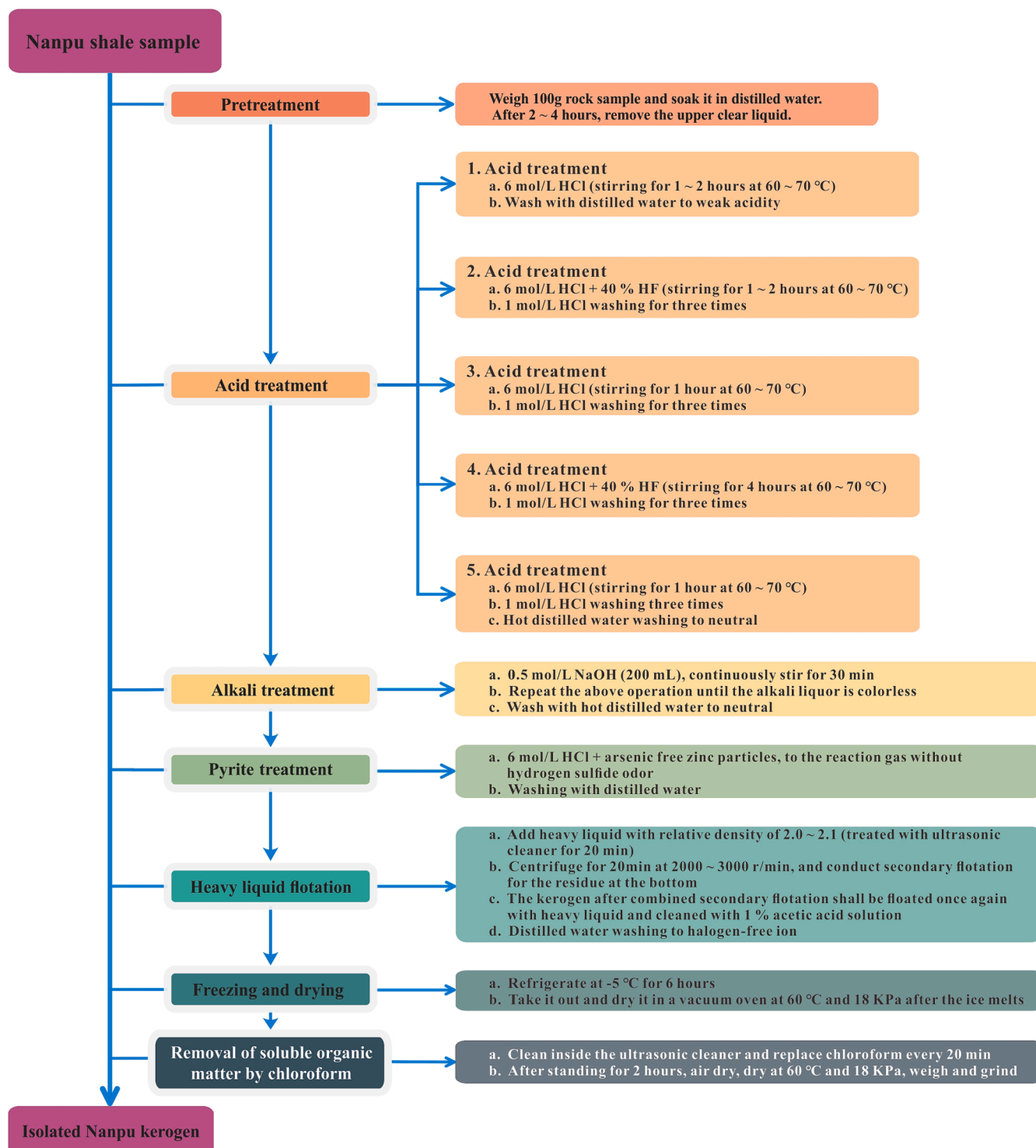


Fig. 2. Flow Chart of Careful Preparation of Kerogen.

kerogen obtained by heavy liquid flotation is washed with distilled water until it is free of halogen ions. The heavy liquid separation step aims to remove heavy metals from rock samples using a heavy liquid medium with a relative density of 2.0–2.1 g/cm³. Place the dried fine-grained kerogen in chloroform and wash it in an ultrasonic cleaner. Replace chloroform every 20 min of cleaning to remove soluble organic matter. After standing for 2 h, the solution appears colorless. Finally, conduct air drying, dry, weigh, grind, and bottle for standby at 60°C and 18 KPa. The final particle size of the obtained kerogen is about 100 mesh. It should be noted here that the long experimental process may have changed the chemical structure of organic matter to some extent [42], so the analysis of extracted kerogen may not give a completely accurate representation of the structure of the organic matter in the original shale.

2.2. Experimental methods

2.2.1. Elemental analysis

Elemental analysis is a chemical analysis method that studies the elemental composition of organic compounds. There are two types of elemental analysis: qualitative elemental analysis and quantitative elemental analysis. The former is used to identify which elements are contained in organic compounds, while the latter is used to determine the percentage content of these elements in organic compounds [44]. A Vario MICRO cube element analyzer from Germany is used to measure the element content and atomic ratio of C, H, O, N, and S in kerogen.

2.2.2. ¹³C NMR experiment

¹³C NMR experiment can provide qualitative and quantitative component analysis for the type of carbon in the framework of organic compounds, which is of great significance for the identification of the chemical structure characteristics of kerogen [45,46]. The advantage of ¹³C NMR detection for kerogen is that it can eliminate interference from the presence of minerals (except Fe mineral) on the organic structure of kerogen. Because carbon atoms are extremely sensitive to their chemical environment, subtle changes in the surrounding structure can be directly reflected in the carbon spectrum, affecting the chemical shifts of each carbon atom [47]. Therefore, ¹³C NMR analysis of kerogen can yield relatively accurate and high-resolution spectral lines, providing accurate and suitable analysis data for carbon skeleton synthesis [25].

The ¹³C NMR testing device is a Bruker AVANCE III HD from Germany. Parameter setting conditions: probe, 4 mm solid state dual resonance probe, ZrO₂ (equipped with Kei-F) rotor; Rotating speed, 12 kHz; ¹³C resonance frequency, 100.80 MHz; Contact time, 2 ms; Cycle delay, 5 s; Number of data acquisition points, 2048. The testing instrument adopts cross-polarization and magic angle spinning technology, with a hydrocarbon cross-polarization contact time of 2 ms and a magic angle spinning frequency of 12 kHz.

2.2.3. FTIR experiment

The most widely used application of FTIR is to analyze the chemical composition of substances qualitatively and quantitatively [48]. Infrared spectroscopy has the advantage, like ¹³C NMR, of causing no structural damage to the experimental sample and avoiding the impact of external chemical reactions on the test structure. At the same time, this method has high sensitivity and speed. It can determine the chemical structure of the contained groups based on the infrared characteristic peaks and group frequencies of different substances in the mixture [49]. The position of its vibration absorption peak is relatively fixed for the same type of chemical bond. Therefore, it is feasible and effective to study the type and content of chemical or active functional groups of oil parent materials through infrared spectroscopy detection [50].

The Bruker ALPHA Fourier infrared spectrometer was used to measure the infrared spectrum. The sample processing for infrared analysis is as follows: 2.5 mg of kerogen concentrate were mixed with 200 mg potassium bromide and ground in an agate mortar. 60 mg of the ground

mixture was pressed into thin sheets under a pressure of 10 MPa, and dried for 6 h under nitrogen at 60°C. The accuracy of the infrared spectrum is 2 cm⁻¹. The Spectral resolution is 4 cm⁻¹, and the wave-number range is 400 to 4000 cm⁻¹. The experiment was completed in transmission mode. The number of scans is 16. Baseline correction was performed. The results are reported using absorbance.

2.2.4. XPS experiment

XPS is a method for analyzing and detecting samples' atomic valence states and molecular structures [51]. When compared to other spectral detection methods, it is possible to better provide structural parameters such as the occurrence type, molecular structure, chemical bonds, and concentrations of heteroatoms in the molecular structure of oil matrix due to its ability to measure electronic information such as atomic inner layer valence and chemical displacement in the structure. At the same time, XPS often does not seriously perturb the surface structure, which is helpful for quantitative and qualitative analysis of organic macromolecular structures. It can provide an accurate and effective experimental basis for the design of O, N, and S atoms in the molecular structure model of the oil matrix [44]. However, it is important to note that XPS is a surface analysis method that provides the atomic valence state and molecular structure of the sample surface (less than 5 nm depth) rather than the whole sample.

Nexsa is an XPS testing instrument manufactured by Thermo Fisher Company in the United States. Parameter setting conditions: monochromatic X-ray, aluminum anode target (K α Radiation); Working voltage, 15 kV; Emission current, 10 mA. The wide scan Pass Energy is 100 eV and the energy step size is 1 eV. The narrow scan Pass Energy is 30 eV and the energy step size is 0.1 eV. The scanning speed is 2°/min, and the scanning range is 2° – 90°; The acquisition speed is 0.3 s/step, and the acquisition step size is 0.02°.

2.2.5. CO₂ adsorption experiment

CO₂ adsorption tests can measure specific surface area, pore volume, pore size distribution, etc. CO₂ adsorption tests mainly reflect micropore information [52]. Compared with Langmuir model which assumes saturation after monolayer adsorption and BET model which assumes multi-layer adsorption, Density Functional Theory (DFT) Method is more suitable for gas adsorption in micropores [52]. Assume that the total isotherm constitutes lots of individual "single pore" isotherms multiplied by their relative PSD. Through the correlation between theoretical adsorption isotherm ($N(P/P_o)$) and experimental adsorption isotherm, the PSD can be obtained [53].

$$N\left(\frac{P}{P_o}\right) = \int_{W_{MIN}}^{W_{MAX}} N\left(\frac{P}{P_o}, W\right) \bullet f(W) dW \quad (1)$$

Where $N(P/P_o)$ = experimental adsorption isotherm data, W = pore width, $N(P/P_o, W)$ = isotherm on a single pore of width W and $f(W)$ = pore size distribution function.

A set of individual "single pore" isotherms ($N(P/P_o, W)$) of width W can be obtained by DFT theory [54]. In this study, The CO₂ adsorption isotherms were analyzed using Density functional theory (DFT) to provide an accurate pore size distribution, thus obtaining pore volume and surface area.

CO₂ adsorption was carried out using a MacASAP 2460 device at 273 K to characterize the pore structure of the sample at less than 2 nm. The crushed sample was dried in an oven at 110°C for 24 h to reduce the impact of free water and volatile gases. It should be noted that during the drying process of kerogen, it can lead to the volatilization of kerogen, but this volatilization is not important. Pretreatment: heating and vacuuming the sample; Record the weight of the sample after degassing; After degassing, reweigh the total weight of the sample tube, sample, and plug assembly, and then subtract the weight of the empty sample tube and plug, and record the weight of the sample; Carry out adsorption experiments, set parameters such as equilibrium relative pressure points

and experimental conditions, continuously inject carbon dioxide gas, and the equipment automatically records the adsorption amount of the sample at different equilibrium relative pressure points. The saturated vapor pressure of CO₂ is 3.48 MPa.

2.2.6. Laser Raman experiment

With the development of laser Raman spectroscopy technology, it has become a relatively mature analysis and testing method, which can play an essential role in fluid inclusions, sedimentary organic matter, and rock ore identification. It has the advantages of simple sample preparation, convenient and rapid testing, and short cycle time. Xiang et al. (2019) first used the drift coefficient to quantify the degree of fluorescence interference related to the coalification degree for dozens of coal samples [55]. Raman spectroscopy-based mineralogical studies can elucidate the changes in crystalline structures of manganate minerals in response to the growth of ferromanganese nodules [56]. There is a proportional relationship between the intensity of the characteristic peaks in Raman spectroscopy and the concentration of the substance. By correcting the intensity parameters of the characteristic peaks, quantitative analysis information of fluid inclusions (relative percentage content of moles) can be obtained [57]. In terms of thermal maturity, the Raman reflectance of samples can be calculated using the kerogen's peak spacing and height ratio, solid asphalt, carbonized animal and plant fossils, and solid organic matter in mineral inclusions [28].

The LabRAM HP Evolution instrument from HORIBA Corporation of Japan is the testing instrument. Spectral range: 200–2100 nm. Laser: 532 nm. Focal length: 800 mm. The wavelength used is 532 nm, and the instrument setup allows a spectral resolution of 4 cm⁻¹. We used a scanning time of 20 s of spectrum in an extending mode spanning 100–4000 cm⁻¹ with a grating of 1800 gmm⁻¹.

2.2.7. Scanning transmission electron microscope (STEM) experiment

Field emission transmission electron microscopy is mainly used to analyze the internal microstructure of materials. Using methods including HRTEM, STEM, Element mapping, and EDX, it can perform microscopic analysis of the morphology, crystal structures, chemical composition, interface, and crystal defects of samples [28]. STEM is becoming an increasingly important electron microscope due to its combination of transmission electron microscopy and scanning electron microscopy functions. Liu et al. (2021) observed the morphology of kerogen particles using TEM and found that the kerogen particles were significantly clustered together, with rough surfaces and nanopores present in the particles [28]. Qian et al. (2020) characterized the morphology and structure of the synthesized materials using STEM [58].

The STEM of the kerogen sample was obtained using the Japanese electronic JEM 2100F instrument. STEM resolution: 0.20 nm. Electron acceleration voltage was 200 kV, spherical aberration coefficient was 0.5 mm, and point resolution and line resolution were 0.19 nm and 0.14 nm, respectively. The STEM images were performed at an electron accelerating voltage of 300 kV with a probe convergence angle of 17.8 mrad.

2.2.8. True density test experiment

True density refers to the actual mass per unit volume of solid material in an absolutely dense state, that is, the density after removing internal pores between particles [59]. Use the gas volume method to measure true density. The gas volume method is to measure the volume of the sample to be tested based on the measured pressure, and then measure the density of the sample based on its mass. This method utilizes helium gas (a small molecular diameter inert gas with easy diffusion, good permeability, and stability) to penetrate into the internal pores of the material, quickly filling the pores of the material that cannot be measured by conventional methods. The sample volume measured by this method will be closer to the true volume of the sample, thus making the true density value of the sample closer to the true value [60]. The true density is calculated as follows:

$$\rho = \frac{m}{V} \quad (2)$$

Where ρ is the true density, m is the mass of the sample, and V is the volume of the sample.

Use AccuPyc II 1345 true density tester for measurement. Method: Place the sample in a true density tester, use helium as the medium, gradually pressurize it to a specified value in the measurement chamber, and then helium expands into the expansion chamber. The equilibrium pressure of the two processes is automatically recorded by the instrument. According to the Conservation of mass, the volume of the measurement chamber and expansion chamber is calibrated by the standard ball, then the volume of the sample is determined, and the true density is calculated. Parameter setting: Sample mass, 1.4919 g; Test temperature 298 K; The volume is 1.2622 cm³; Expansion volume: 8.4450 cm³.

2.3. Method for constructing the average molecular structure of kerogen

Due to the complexity and irregularity of the molecular structure of shale kerogen, it is impossible to construct a model that conforms to all the physicochemical properties. Therefore, the concept of the "average molecular structure model" [25] was introduced to study some chemical or physical properties of shale kerogen. Based on experimental data such as elemental analysis, XPS, FTIR, and ¹³C NMR, an average molecular structure model that can represent the kerogen of the Nanpu shale is constructed, which is summarized in seven steps (Fig. 3).

Step 1: Information on the carbon skeleton structure, aliphatic structure, and aromatic structure of kerogen is obtained by analyzing experimental data such as elemental analysis, XPS, FTIR, and ¹³C NMR.

Step 2: Based on the information obtained in Step 1, the molecular fragments are spliced using ChemDraw software to obtain a preliminary 2D structure of kerogen.

Step 3: The structure of 2D kerogen is obtained based on experimental results such as elemental analysis, XPS, FTIR, and ¹³C NMR. Therefore, the ¹³C NMR spectrum of 2D kerogen may not be consistent with the ¹³C NMR results measured in the experiment. Analyze the 2D structure of kerogen obtained in Step 2 using MestRenova software for ¹³C NMR spectroscopy and compare it with the spectrum obtained from the experimental results.

Step 4: Constantly adjust the structure of 2D kerogen based on the difference between the ¹³C NMR spectrum obtained from the 2D structure of kerogen and the experimental results.

Step 5: Until the ¹³C NMR spectrum obtained from the 2D structure of kerogen coincides with the curve of the spectrum obtained from the experimental results, the final 2D structure of kerogen is obtained.

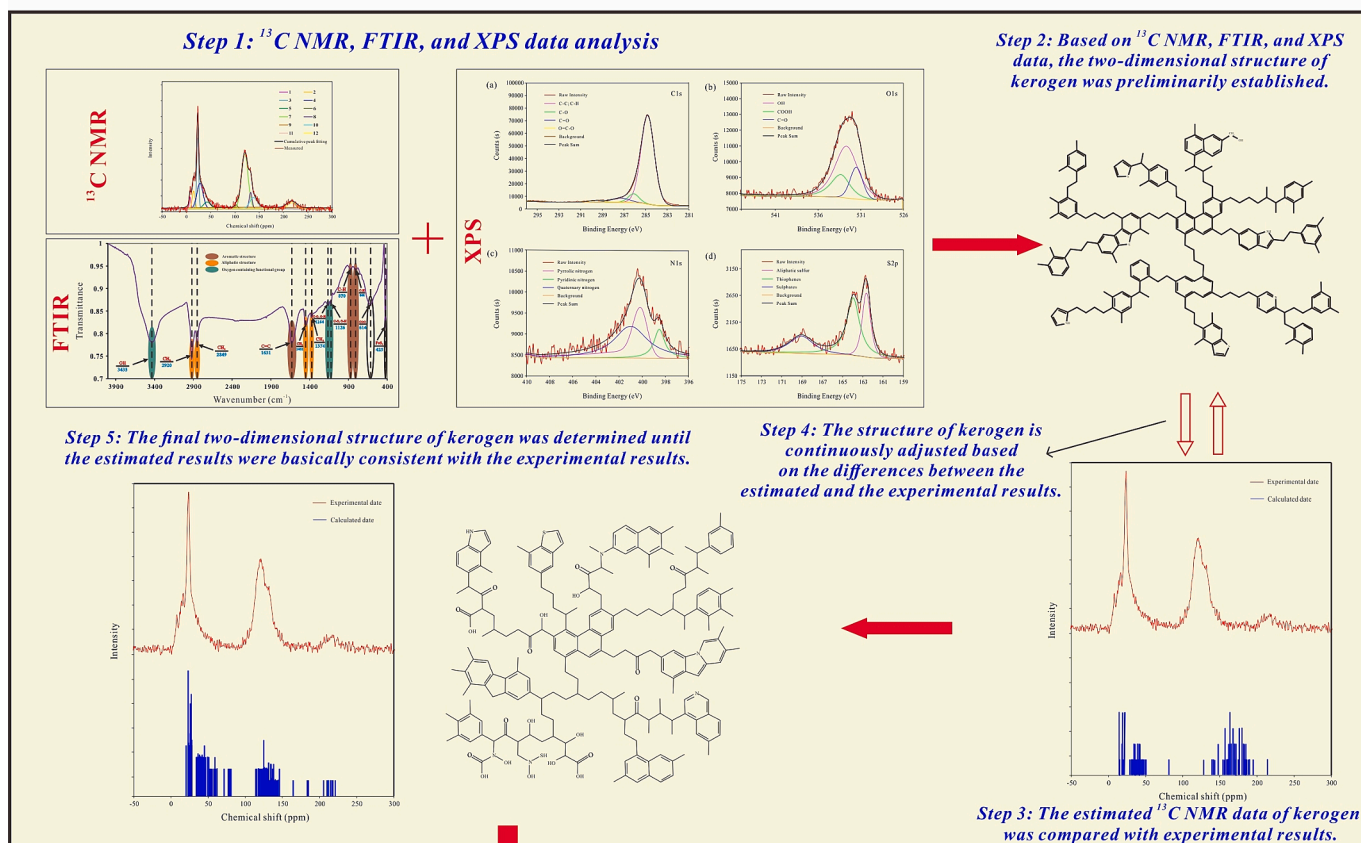
Step 6: Import the final 2D structure of kerogen into Materials Studio, and after a series of operations such as optimization and annealing, obtain the 3D structure of kerogen.

Step 7: Use the Amorphous Cell module in Materials Studio to put multiple 3D structures into a box and then continuously conduct dynamic simulation until it is concluded that the density of 3D kerogen is almost the same as the actual density of kerogen. Then the final 3D structure model of kerogen is obtained.

2.4. ReaxFF MD simulation

The reaction force field uses the idea of molecular mechanics to describe the interaction potential between atoms. It can be used to calculate for example small molecule reactions, combustion, explosion, and transition metal catalysis. ReaxFF is two orders of magnitude slower than a general force field, and takes and its time consumption is between those of simple molecular force fields those of semi-empirical quantum chemical methods. It can be used to calculate thousands or tens of thousands of atoms [61]. The expression of reaction force field energy is as follows:

2D kerogen model



3D kerogen model

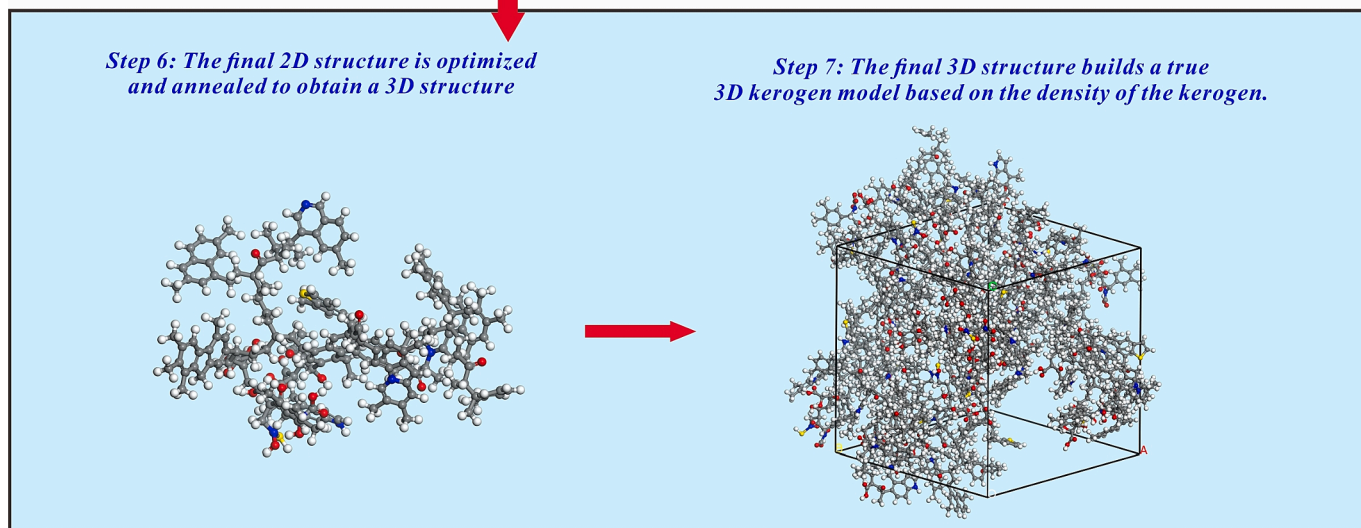


Fig. 3. Construction process of average molecular structure model of kerogen.

$$E_{\text{total}} = E_{\text{valence}} + E_{\text{crossterm}} + E_{\text{nonbond}} \quad (3)$$

Where E_{valence} is composed of chemical bond stretching energy, bond angle bending energy, dihedral angle torsion energy, etc., $E_{\text{crossterm}}$ represents the coupling cross terms between bonds and angles, and E_{nonbond} takes account of weak interactions such as those due to van der Waals energy, hydrogen bond energy, etc.

MD deals with the motion of particles based on classical mechanics. The finite difference method is used for the numerical integration of equations of motion. At present, there are no computational limits in

simulating complex biological macromolecular systems due to the continual maturation of MD simulation technologies.

ReaxFF MD does not require a predefined reaction path and enhances computation accuracy by dynamically optimizing atomic charge. Moreover, the simulated system can have more than 1000 atoms. After determining the molecular model and setting technical parameters such as periodic boundary conditions, integration time steps, simulation ensemble, state variables (P, T, V), simulation steps, and information to be output, formal simulation can be conducted.

This study used ReaxFF MD to simulate the pyrolysis of kerogen. The specific parameter settings are as follows: the periodic boundary is $3.597 \text{ nm} \times 3.597 \text{ nm} \times 3.597 \text{ nm}$; Simulate a time step of 0.25 fs, with a total of 1,000,000 steps; Select NVT ensemble and H/C/O/N/S/B force field. The pyrolysis temperatures are set at 1500 K, 2000 K, 2500 K, 3000 K, 3500 K, 4000 K, 4500 K, and 5000 K, respectively, and the heating rates are set at 20 K/ps.

3. Results

3.1. Carbon skeleton structure information of kerogen

The skeleton of kerogen is made up primarily of C, making ^{13}C NMR spectroscopy a key technology for studying the structure of kerogen. This technology can reflect the overview of the carbon skeleton structure in kerogen [25,45,46]. The ^{13}C NMR spectrum of kerogen from the Nanpu shale can be divided into three major categories: aliphatic carbon (0–90 ppm), aromatic carbon (90–170 ppm), and carbonyl carbon (170–220 ppm) (Fig. 4) [62,63]. We can see that aliphatic and aromatic groups make up most of the spectrum. The principal peaks in the aliphatic groups are attributed to aromatic methyl carbon, methylene carbon, and multi-branched center carbon [64]. The FTIR spectrum in Section 3.2 provides further support for the above NMR interpretation.

In order to determine the relative fraction of different carbon forms in the kerogen of the Nanpu shale, the ^{13}C NMR curve was fitted using Origin software (Fig. 4 and Table 1). The following conclusions can be drawn through analysis:

(1) Among the average 100 carbon atoms in the molecular structure, there are about 6 terminal aliphatic methyl groups, while the methylene carbon connected to the terminal methyl group is 0, indicating that there are 6 non-chain aliphatic methyl groups.

(2) The components of the aromatic structure: According to ^{13}C NMR data, there are approximately 55 total aromatic carbons, 31 proton aromatic carbons, 4 bridged aromatic carbons, and approximately 20 alkyl-substituted aromatic carbons.

(3) The components of aliphatic structure: calculated from ^{13}C NMR data, the number of terminal methyl groups is about 6, the number of

aromatic methyl groups is about 11, and the number of methylene groups is about 11.

After calculation, the following structural parameters of kerogen from the Nanpu shale kerogen can also be obtained:

(1) Carbon Aromaticity: From the ^{13}C NMR (CP/MAS) spectrum of kerogen, the boundary between the chemical shift between aliphatic carbon and aromatic carbon is between 95 and 100 ppm. The aromatic carbon ratio is defined as the fraction of aromatic carbon in the total carbon content, which can be calculated from the fraction of the 95–164 ppm signal intensity integral value in the ^{13}C NMR spectrum to the total signal intensity value.

$$f_a = f_{ar}^H + f_{ar}^B + f_{ar}^C = 54.67 \quad (4)$$

(2) The percentage of alkyl carbon is the percentage of aliphatic carbon in the total carbon content.

$$f_{al} = f_{al}^M + f_{al}^A + f_{al}^H + f_{al}^D = 40.13 \quad (5)$$

This indicates that the main molecular structures of kerogen are aromatic and aliphatic chain structures.

3.2. Molecular fragments and functional group analysis of kerogen

3.2.1. FTIR experimental results

The composition, relative abundance, and bonding characteristics of chemical groups in kerogen can be studied using the location and relative strength of infrared absorption peaks. [48]. Fig. 5 depicts the FTIR curve of kerogen from the Nanpu shale. The main spectral bands are as follows: 2920 cm^{-1} , 2849 cm^{-1} , 1451 cm^{-1} , and 1374 cm^{-1} (saturated hydrocarbon structure); 1631 cm^{-1} , 870 cm^{-1} , and 808 cm^{-1} (aromatic hydrocarbon structure); 3433 cm^{-1} , 1164 cm^{-1} , 1126 cm^{-1} , 614 cm^{-1} (oxygen atom structure).

Three main peaks attributable to aromatic carbon, methylene carbon, and –OH were seen in the vicinity of 1600 cm^{-1} , 2900 cm^{-1} , and 3400 cm^{-1} , respectively [65]. The 2920 cm^{-1} and 2849 cm^{-1} spectra indicate an antisymmetric and symmetrically stretched frequency band of aliphatic methylene ($-\text{CH}_2-$) [62], consistent with the methylene signal (at 30 ppm) dominating the ^{13}C NMR spectrum. In addition, the

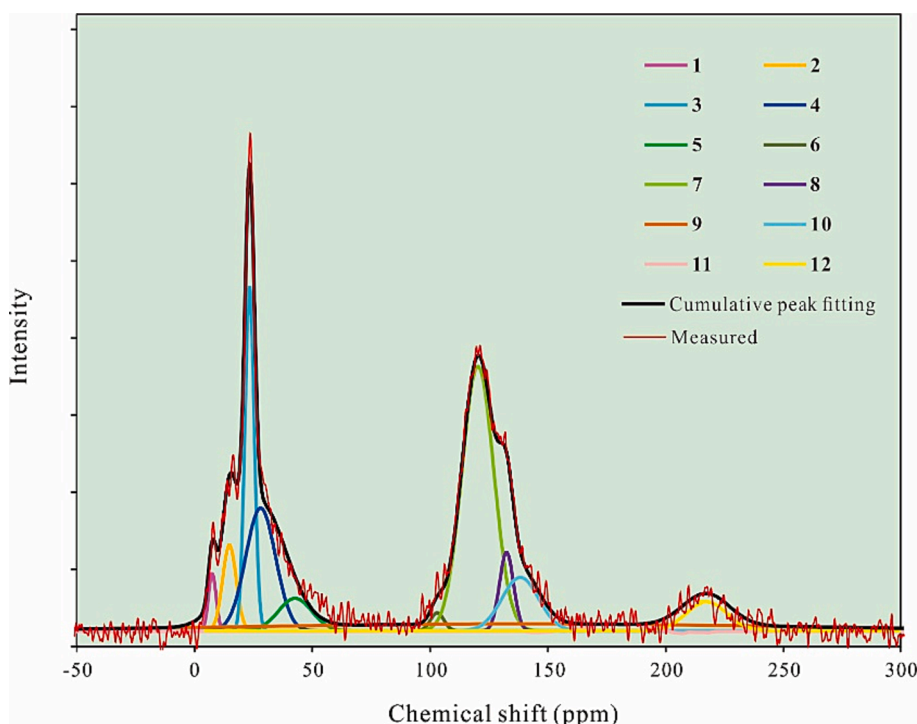
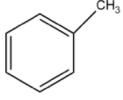
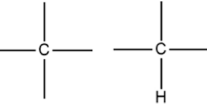
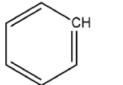
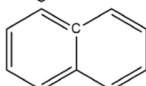
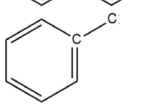
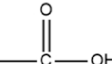

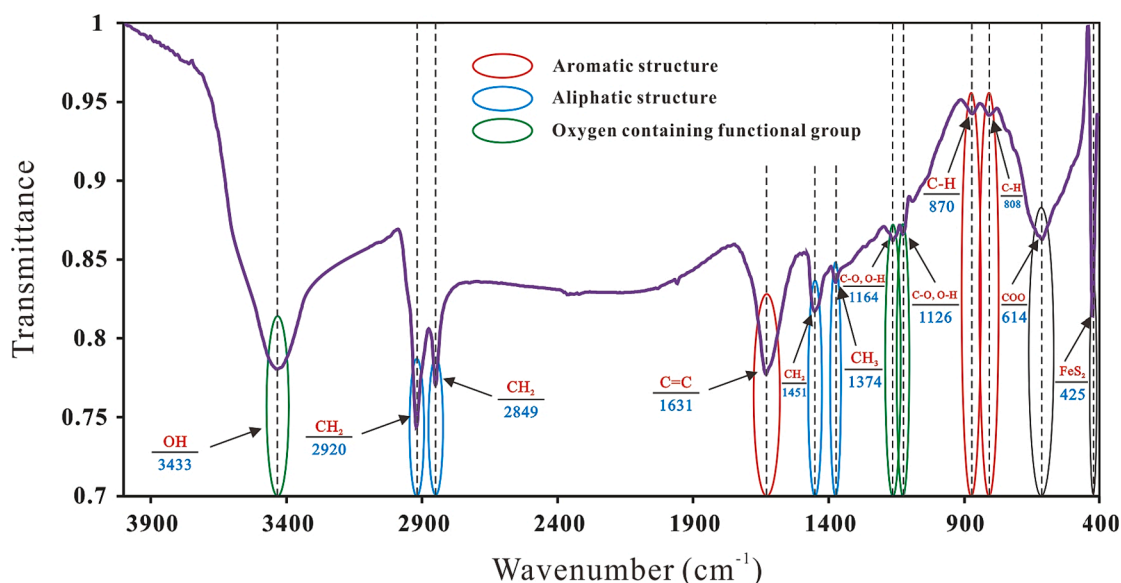


Fig. 4. ^{13}C NMR spectrum and fitting curve of kerogen from Nanpu shale kerogen.

Table 1Chemical shifts and distribution parameters of different types of carbon determined by solid ^{13}C NMR.

Peak	Area	Chemical shift	Symbol	Ratio%	Location	Carbon type
1	1.51E + 03	7	f_{al}^{M}	1.54	$-\text{CH}_3$	Terminal methyl carbon
2	4.03E + 03	14.8	f_{al}^{M}	4.12		
3	1.11E + 04	23.45	f_{al}^{M}	11.29		Aromatic methyl carbon
4	1.08E + 04	28.11	f_{al}^{H}	11.02	$-\text{CH}_2-\text{CH}_2-\text{CH}_2-$	Methylene carbon
5	1.19E + 04	42.72	f_{al}^{H}	12.16		Multi branched central carbon (quaternary carbon, tertiary carbon)
6	8.39E + 02	103	f_{ar}^{H}	0.86		Proton aromatic carbon
7	2.90E + 04	120	f_{ar}^{H}	29.63		
8	3.80E + 03	132	f_{ar}^{B}	3.88		Bridged aromatic carbon
9	6.79E + 03	138.32	f_{ar}^{C}	6.93		
10	1.37 E + 04	138.32	f_{ar}^{C}	13.37		Alkyl substituted aromatic carbon
11	1.16E + 03	178	f_{a}^{C}	1.20		Carboxylic carbon
12	3.92E + 03	217	f_{a}^{O}	4.00		Carbonyl carbon

**Fig. 5.** FTIR spectrum of kerogen sample.

presence of ether groups (C–O or C–O–C) in the structure was demonstrated at 1164 cm^{-1} ; 3433 cm^{-1} is the vibration frequency band of hydroxyl (–OH). The bands of aromatic hydrocarbon structures are weaker than those of saturated hydrocarbons. The kerogen preparation procedure is lengthy, and entirely removing minerals is challenging. Oil shale primarily contains silicate minerals such as kaolinite, quartz, illite, etc. Their presence can substantially interfere with the absorption of oxygen containing groups (ether, ester) and the out-of-plane flexural vibration bands of aromatic hydrocarbons.

3.2.2. XPS experimental results

The occurrence mode and relative content of oxygen, nitrogen, and sulfur elements in the organic structure of kerogen were obtained by fitting the XPS spectra of kerogen samples by peak division (Fig. 6, Table 2, and Table 3); taking the attribution of each characteristic peak in the literature as a reference [28,51]. The main C1s peak was obtained at 284.8 eV and the main O1s peak was obtained at 532.66 eV (Table 3). Due to the absence of nitrogen oxides, pyrite, and other minerals in shale organic kerogen, the XPS data were normalized to 90.6% and 5.9% carbon and oxygen, 2.5% nitrogen, and 1.0% sulfur, respectively (Table 2).

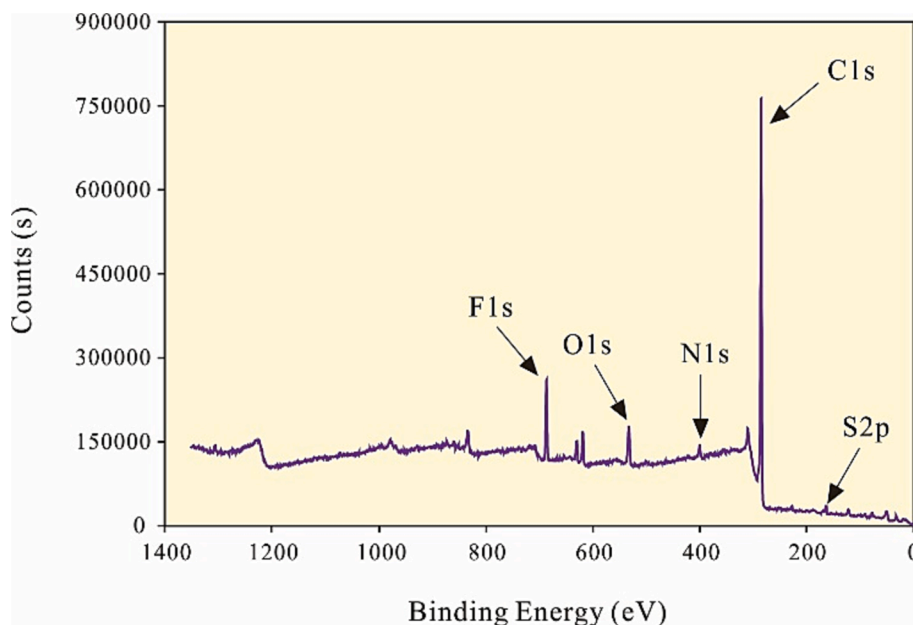


Fig. 6. XPS spectrum of kerogen from Nanpu shale.

Table 2
XPS data of kerogen from Nanpu shale.

Name	Peak	FWHM	Area	Atomic %
C1s	285.08	2.62	1801394.05	90.6
O1s	532.82	4.02	282437.13	5.9
N1s	400.06	3.33	76677.64	2.5
S2p	163.39	2.01	39047.28	1.0

Fig. 7 and Table 3 show the XPS peak fitting spectrum of kerogen from the Nanpu shale and the proportions of different bond types. The carbon atoms in the form of C–C and C–H bonds account for over 80% of the total carbon. Some carbon atoms also exist as O = C–O (1.9%), indicating traces of carboxylic groups in the structure of kerogen. More than half of the oxygen atoms are in the form of –OH (59.0%). The oxygen atoms in the carbonyl group account for 17.6% of the total oxygen atoms. The oxygen atoms in the carboxyl group account for 23.4% of the total oxygen atoms. According to XPS data, nitrogen atoms in kerogen mainly exist in the form of amines, accounting for approximately 48.0% of the total nitrogen atoms. There are also some pyrrole nitrogen atoms

and pyridine nitrogen atoms, with ratios of 36.8% and 15.2%, respectively. The S element in kerogen mainly exists in the form of aliphatic sulfur and thiophene. The sulfur atoms of aliphatic sulfur account for 38.8% of the total sulfur atoms. The sulfur atoms on thiophene account for 30.4% of the total sulfur atoms. However, it is important to note that XPS is a surface analysis method that provides the atomic valence state and molecular structure of the sample surface rather than the whole sample. Therefore, there will be a certain amount of adventitious carbon, which mainly exists in the form of C–O (Table 3). And by comparing the XPS with the results obtained from elemental analysis, it can be found that the proportion of nitrogen measured by XPS is higher than that measured by elemental analysis. This indicates that the surface nitrogen content of the sample is slightly higher, and the relative proportion of nitrogen functional groups inferred from XPS is slightly higher.

3.2.3. Elemental analysis experimental results

Shale kerogen is a 3D heterogeneous complex with complex structures without fixed molecular weights and structural formulas. Therefore, the molecular structure model designed represents the average

Table 3
Peak fitting results of XPS.

Name	Position(eV)	Area	FWHM (eV)	Atomic	Functional group	Structural formula
C1s	284.8	110533.49	1.51	85.9%	/	C–C; C–H
	286.1	8822.7	1.22	6.9%	/	C–O
	287.3	6840.02	1.94	5.3%	Carbonyl	O = C
	289.5	2437.33	1.68	1.9%	Carboxyl	O = C–O
O1s	532.66	12463.56	3.26	59.0%	/	–OH
	533.31	4935.98	2.57	23.4%	/	–COOH
	531.49	3728.79	1.77	17.6%	Carboxyl	C = O
	531.49	3728.79	1.77	17.6%	Carboxyl	C = O
N1s	400.18	2723.16	1.44	36.8%	Pyrrole nitrogen	
	398.52	1129.69	1.09	15.2%	Pyridine nitrogen	
S2p	400.94	3557.29	3.38	48.0%	Quaternary amine	R–N–R
	162.62	1369.64	0.97	38.8%	Aliphatic sulfur	R–SH
	163.94	1074.4	1.51	30.4%	Thiophenes	
	169.04	1089.6	2.87	30.8%	Sulfate	

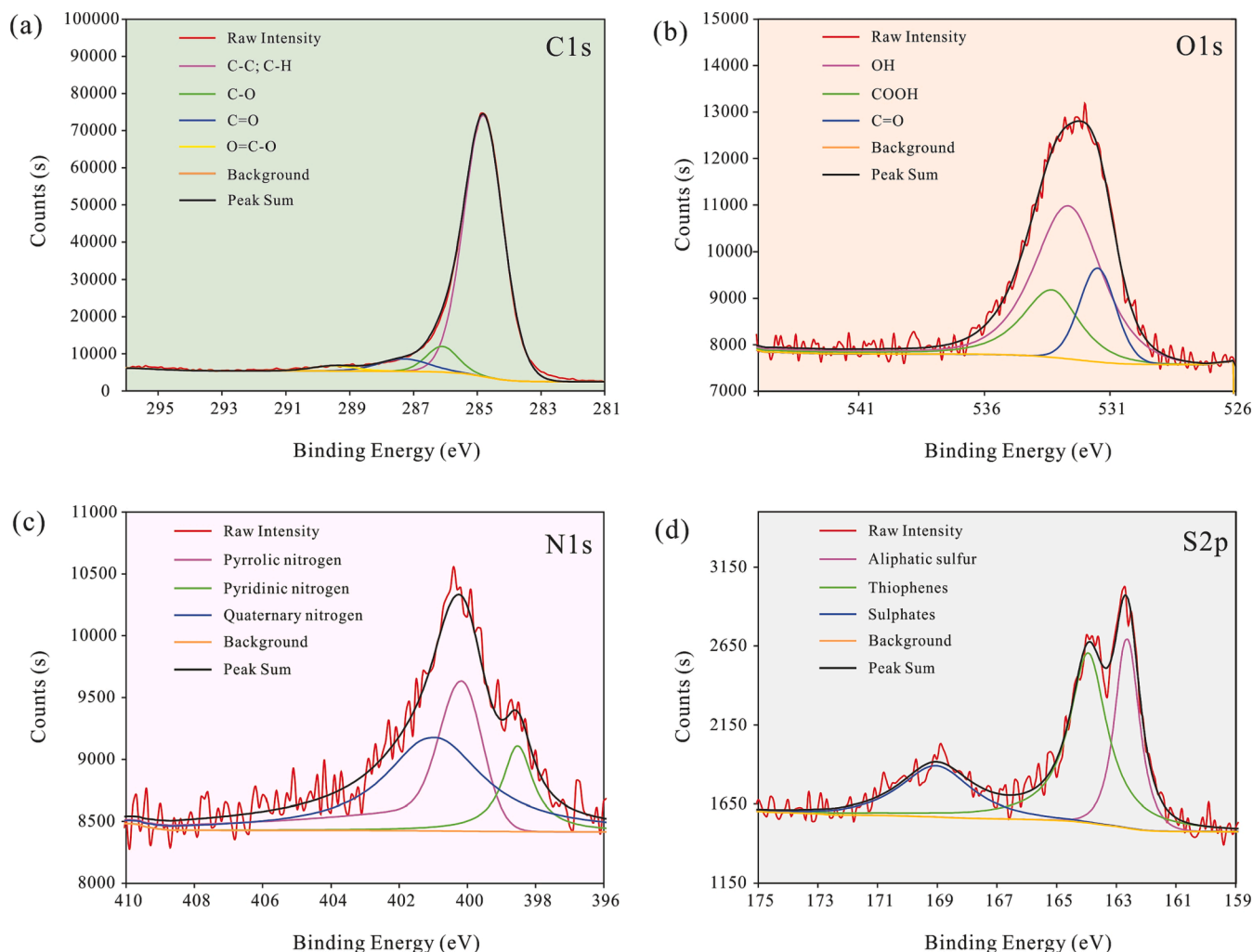


Fig. 7. XPS peak fitting spectrum of kerogen from Nanpu shale (a) C1s scanning; (b) O1s scanning; (c) N1s scan; (d) S2p scan.

molecule of kerogen. The interaction between shale kerogen and inorganic matrix [66] leads to the tight binding between kerogen and minerals, making it difficult to completely separate shale kerogen [67,68,69]. The actual measured total amount of these five elements is less than 100%. Thus, a normalization correction has been applied in this research based on the experimental data of shale kerogen, as shown in Table 4.

3.3. Construction and verification of 2D structural model of kerogen

Structural parameters of shale kerogen in Nanpu Sag were obtained based on elemental analysis, ^{13}C NMR, FTIR, and XPS. The kerogen structure of the Nanpu shale is mainly composed of aliphatic and aromatic structures. The nitrogen element is present in the kerogen as pyrrole, pyridine, and quaternary amine. The sulfur element and its compounds are mainly present in the kerogen as aliphatic sulfur and thiophene. The construction process is as follows:

From the normalized XPS parameters, the ratio of pyrrole, pyridine, and the quaternary amine is about 3.7:1.5:4.8. To make the constructed

kerogen model more consistent with the actual characteristics of kerogen, it is determined that the number of amines is 3, pyrrole is 2, pyridine is 1, and the total nitrogen atom is 6. Based on elemental analysis data and atomic number ratio, the total number of Cs inversely estimated is about 200. In addition, Table 3 and 4 indicate that there are 1 thiophene and 1 aliphatic sulfur for every 200 Cs. At the same time, the number of oxygen atoms is calculated to be 20, based on the atomic ratio. According to ^{13}C NMR data, there are 3 carboxyl groups, and 7 carbonyl groups, and the remaining O atoms are most simply assigned to -OH, but the ^{13}C NMR would not support such an assignment, so that the matter remains doubtful.

Table 1 shows the number of terminal methyl carbon, aromatic cyclomethyl carbon, methylene carbon, multi-branched center carbon, proton aromatic carbon, bridged aromatic carbon, alkyl-substituted aromatic carbon, carboxyl carbon, and carbonyl carbon that can be obtained in the kerogen structure. Finally, lipid chains connect various aromatic structural units and place functional groups in appropriate positions. The molecular plane model of kerogen was drawn using ChemDraw software.

Table 4
Element analysis and the atomic ratio of kerogen.

Organic matter					Inorganic matter (%)	O/C (atomic)	H/C (atomic)	N/C (atomic)	S/C (atomic)
C (%)	H (%)	O (%)	N (%)	S (%)					
79.18	5.75	10.33	2.51	2.23	10.65	0.10	0.87	0.03	0.01

Fig. 8 shows the final molecular structure. This molecular model's key characteristic is a network structure of aliphatic and aromatic structures instead of a parallel sheet structure dominated by aromatic structures, like those found in coal molecules. According to the above steps, the chemical formula of the molecular model is $C_{199}H_{240}O_{20}N_6S_2$, and the molecular weight is about 3096 Daltons.

Since ^{13}C NMR spectroscopy maps reflect the general structure of the carbon skeleton in kerogen and are the most critical information for the structural composition of kerogen, they are used as a standard for modifying the structural model. The obtained 2D molecular structure model of kerogen was imported into the nuclear magnetic spectrum simulation software MestRenova for correction calculations. Specific process: (1) Obtain ^{13}C NMR spectra of the kerogen structural model through the MestRenova software; (2) compare the differences between the simulated and the experimental spectra; and (3) correct the 2D structural model of shale kerogen. The specific correction process is shown in Fig. 9.

The construction standard is reached by continuously adjusting the kerogen structure until the constructed shale kerogen structure model

matches the experimental parameters. The final kerogen model is shown in Fig. 8. The characteristics of this model, such as size and degree of condensation, are taken from the average values measured for actual kerogen and correlate well with the experimental structural parameters, as shown in Fig. 10. Therefore, it can be considered that the model established is reasonable and can represent the realistic structure of kerogen molecules in the Nanpu shale.

3.4. Construction of 3D structural model of kerogen

Based on the 2D structure, Materials Studio (MS) was used for geometric optimization and kinetic operation to construct a 3D molecular structure model of the kerogen from the Nanpu shale. Molecules are composed of atoms, and both molecules and atoms exist as systems in nature. Due to the interaction of covalent and non-covalent bonds between atoms and intermolecular forces, the molecular configuration must be 3D. Under natural conditions, all molecules reside in their most stable configuration, i.e., the conformation with the lowest total molecular energy. In this section, the initial stable conformation of the 2D

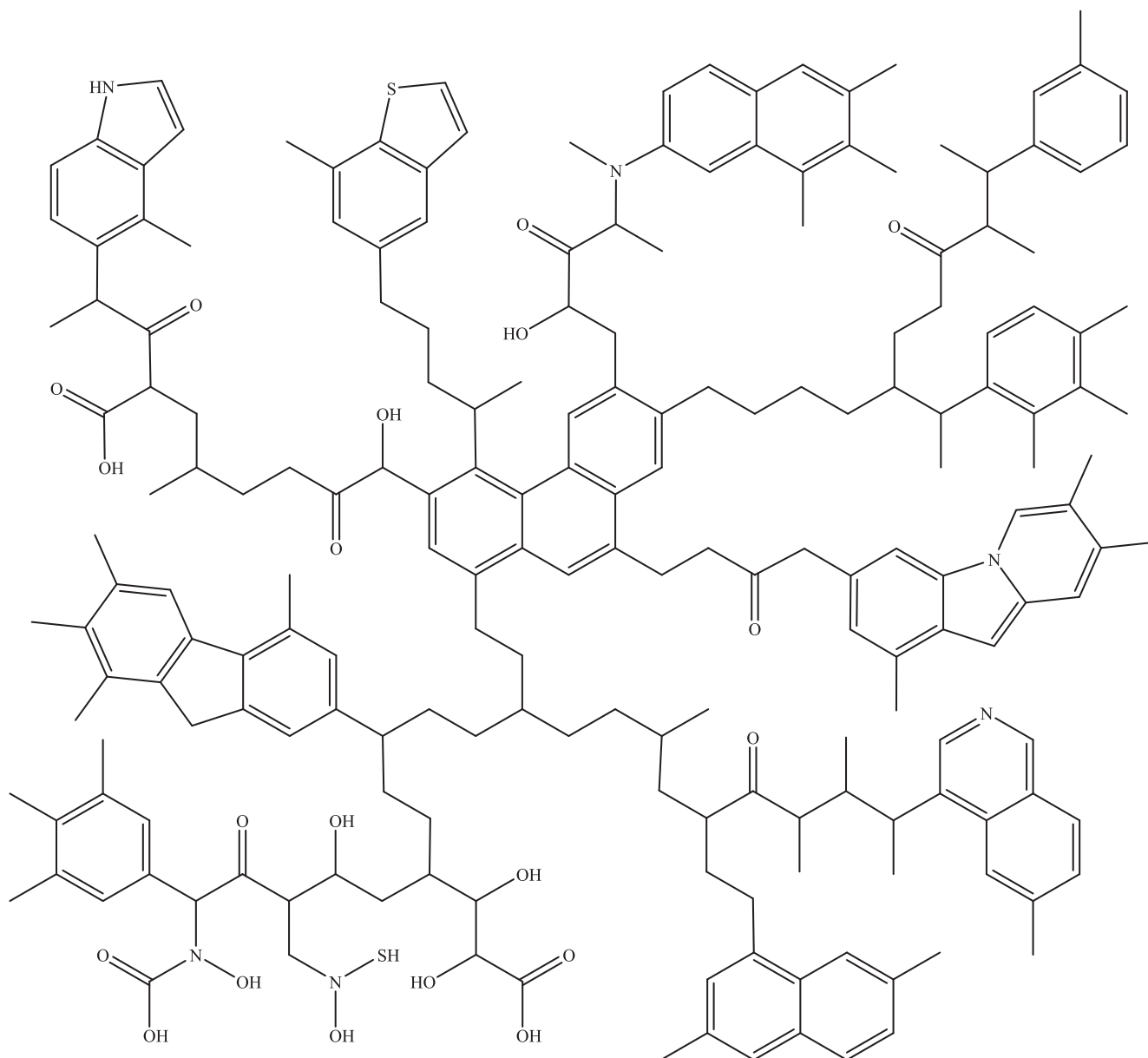


Fig. 8. 2D molecular structure of kerogen from Nanpu shale.

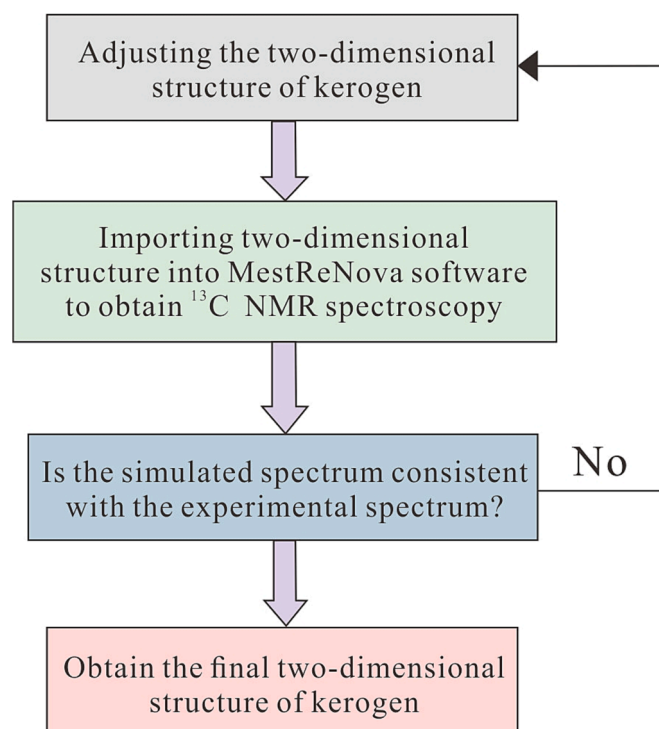


Fig. 9. Flow chart for modification of Nanpu shale kerogen model.

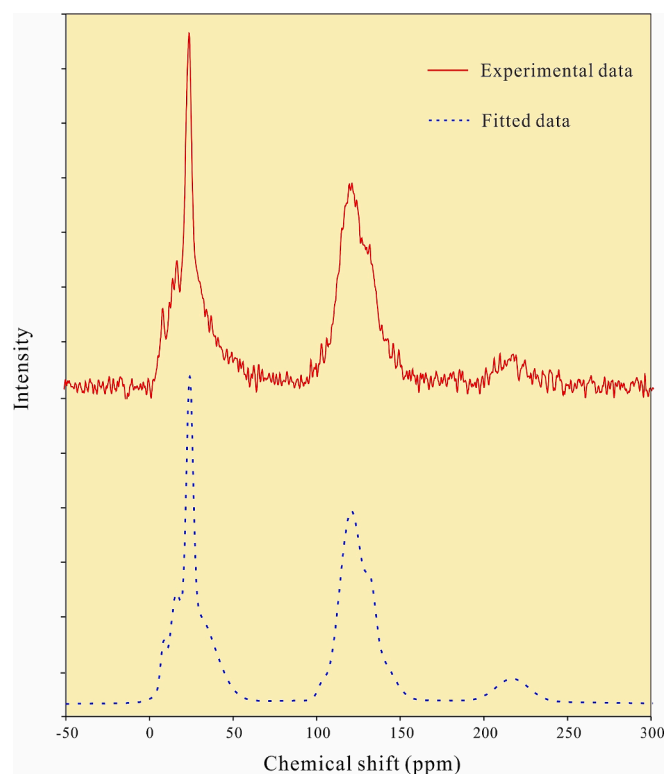


Fig. 10. Comparison of ^{13}C NMR data for experimental and 2D kerogen structure estimation.

model is presented through MD calculations. On this basis, structural optimization and annealing simulation are performed to obtain the optimal configuration of the 3D geometric structure of the model. Dynamic calculations are used to compare the total molecular energies of various 3D geometric configurations that are optimal, and the

configuration with the lowest total energy is ultimately chosen to build a cubic crystal cell with periodic boundary conditions through the Construction task of the Amorphous Cell module as the final 3D average molecular structure model. The construction process and details of the 3D kerogen structure model is shown in [supplementary materials](#).

Through molecular dynamics NVT and NPT ensemble calculations, the variation of the density of the kerogen polymolecular system with temperature was obtained. As shown in [Fig. 11](#), the calculated density at 298 K was 1.106 g/cm^3 . The density of kerogen we measured through experiments is 1.182 g/cm^3 , which is similar to the density of 1.106 g/cm^3 of the established 3D kerogen model, confirming the reliability of our model. The total energy of the system is $13216.544 \text{ kcal/mol}$, $3.597 \text{ nm} \times 3.597 \text{ nm} \times 3.597 \text{ nm}$. The final 3D molecular structure model of kerogen in the crystal cell is shown in [Fig. 12](#). Molecular structure model of 2D and 3D kerogen is shown in [Supplementary Material](#).

3.5. ReaxFF MD simulation of kerogen pyrolysis

The temperature range simulated by ReaxFF MD is often much higher than that of pyrolysis experiments, which does not mean that ReaxFF MD pyrolysis simulation unreliable under experimental temperature conditions. However, along simulation time is required for low temperatures. However, due to computer power restrictions, the simulation process often needs to be completed in picoseconds, which is significantly less than the experimental reaction time. According to the Arrhenius formula, increasing the reaction temperature can significantly increase the reaction rate. Therefore, we often shorten the reaction time by increasing the reaction temperature [70,71,72]. Although there are significant differences in reaction temperature and time between the experimental and simulated processes, the product distribution and kinetic parameters obtained from the simulation are in good agreement with the experimental results [73,74]. This study focuses primarily on how temperature affects the pyrolysis reaction mechanism. Use the 3D structural model of kerogen obtained in [section 3.4 \(Construction of 3D structural model of kerogen\)](#) to conduct molecular dynamics simulation of the reaction. The specific process is shown in [Fig. 13](#).

[Fig. 14](#) shows the number of molecules produced by the pyrolysis of kerogen at different temperatures for a reaction time of 250 ps. As the temperature increases, the slope of the curve gradually increases, the reaction rate accelerates, and the number of molecules ultimately generated also gradually increases. At 1500 K, the number of molecules produced during pyrolysis is very small, indicating that the pyrolysis reaction has not yet occurred at this temperature. At 2000 K, the number of molecules produced by pyrolysis began to increase, ultimately producing 190 molecules. When pyrolysis is carried out at a temperature of 5000 K, the number of molecules gradually increases in the initial stage of the pyrolysis reaction, and the final number of molecules produced during pyrolysis is similar to that under 4500 K, indicating that when the temperature exceeds 5000 K, and the pyrolysis of kerogen is less affected by temperature.

The distribution of gas products by ReaxFF MD simulation at different temperatures is shown in [Fig. 15](#). It can be observed that the quantities of H_2O and H_2 gradually increase with the increase of pyrolysis temperature, especially when the temperature exceeds 2000 K, the generation rate of H_2 significantly increases. As the temperature increases, H_2O and H_2 are greatly affected by temperature, while CO_2 is less affected by temperature. This phenomenon is consistent with the conclusion obtained by Qian et al. (2016) through Reax FF pyrolysis simulation [75].

[Fig. 16](#) shows the variation of different types of pyrolysis products with temperature. It can be seen that temperature is an important factor affecting the composition of pyrolysis products. The generation of liquid products ($\text{C}_5\text{-C}_{40}$) mainly occurs in the low-temperature region. As the temperature increases, the overall number of gaseous hydrocarbons ($\text{C}_1\text{-C}_4$) shows a gradually increasing trend. This is consistent with the trend of changes in the content of gaseous hydrocarbons ($\text{C}_1\text{-C}_4$) that undergo

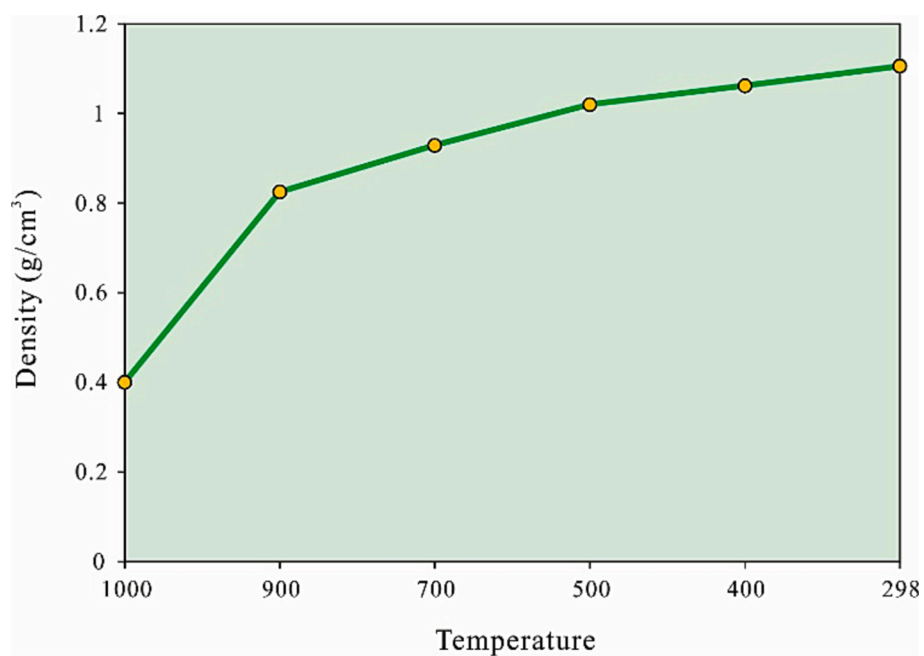


Fig. 11. Evolution curve of the physical density of kerogen macromolecular system.

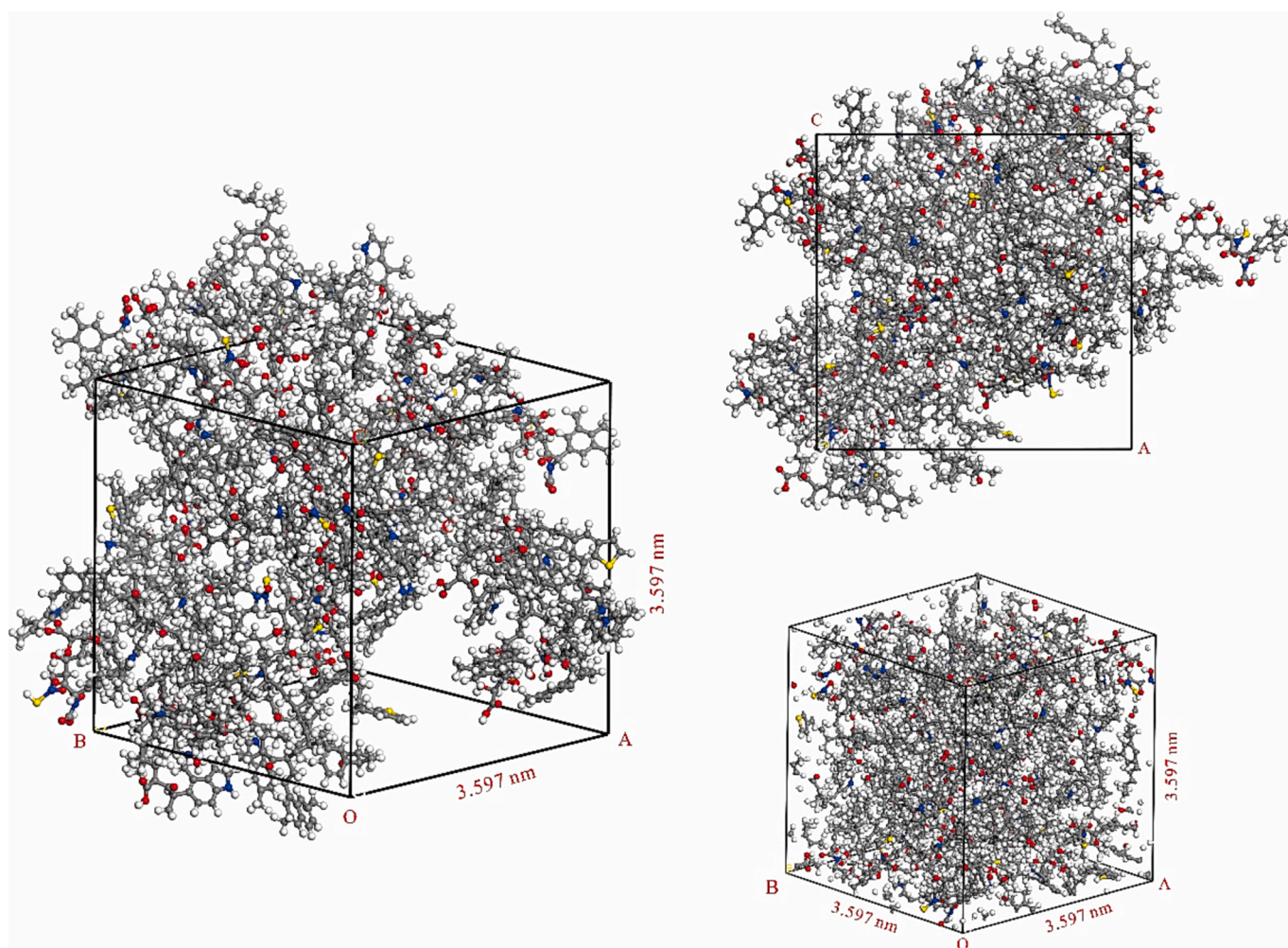


Fig. 12. 3D molecular structure of kerogen in the crystal cell.

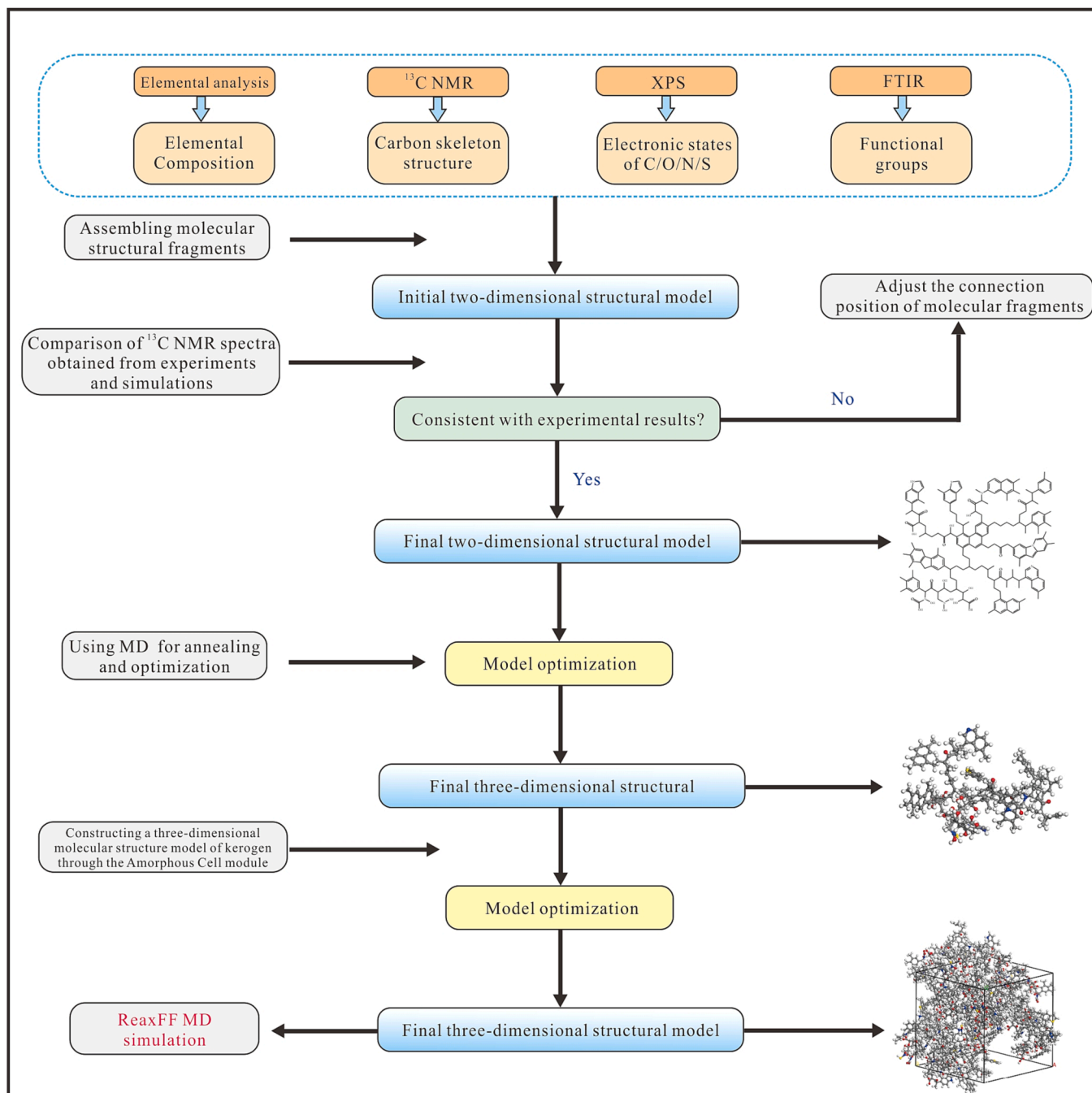


Fig. 13. Construction and pyrolysis process of molecular structure models of kerogen based on various experiments and simulations.

the initial reaction of kerogen in a sealed gold tube system [76,77,78]. The amount of light Shale oil (C₅-C₁₅) increased rapidly from 2000 K, and began to decrease again after 2500 K. Cao et al. (2021) found that the change trend of light Shale oil is consistent with our conclusion through experiments [78]. Xu et al. (2021) believe that this is because the primary pyrolysis of kerogen is gradually completed with the increase of temperature, but the high pyrolysis temperature will lead to the secondary pyrolysis of Shale oil to generate gas, reducing the yield of Shale oil [79]. When the temperature exceeds 2500 K, the quantity of heavy Shale oil (C₁₆-C₄₀) and solid products (C₄₀₊) begins to significantly decrease due to secondary cracking reactions. The evolution trend of the yield of heavy Shale oil obtained by pyrolysis simulation with temperature is also consistent with the experimental results [76,78,80,81].

4. Discussion

4.1. Aggregation morphology and apparent morphology of kerogen

Through STEM images, we can see that the kerogen contains many nanopores, and its borders are thin. (Fig. 17a). We can also directly observe the particles of kerogen, which aggregate with each other, with a rough surface and a bright white color (Fig. 17b).

4.2. Chemical information for kerogen

Using low maturity samples for pyrolysis analysis can more comprehensively characterize the changes in the characteristics of hydrocarbon generation products in kerogen samples [82]. The reflectance

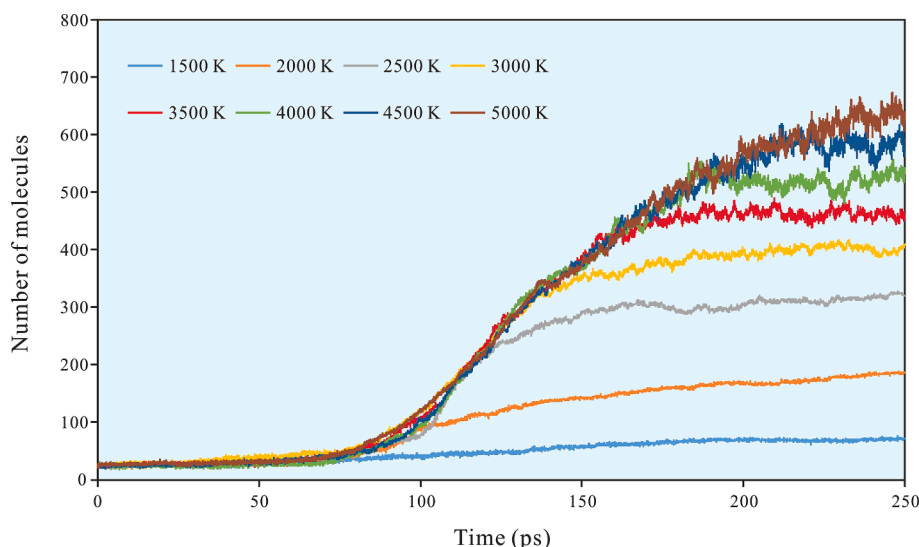


Fig. 14. Molecular numbers obtained from pyrolysis of kerogen at different temperatures.

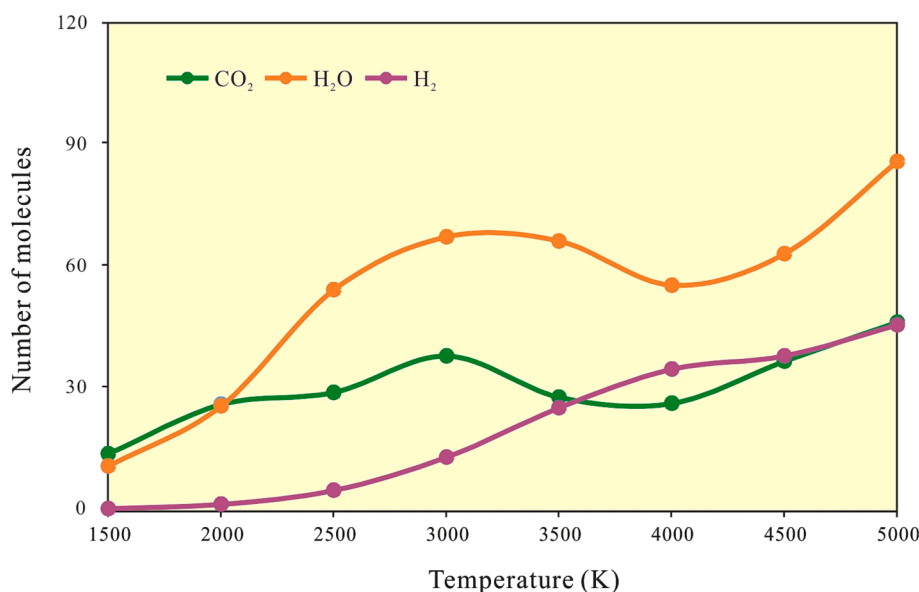


Fig. 15. Changes in gas products from kerogen pyrolysis at different temperatures.

of Vitrinite is a key indicator of maturity. Therefore, we need to measure the Vitrinite reflectance of kerogen. The Raman D band ($1300\text{--}1400\text{ cm}^{-1}$) and G band ($1400\text{--}1500\text{ cm}^{-1}$) positions are closely related to thermal maturity. The D and G bands are located at 1363 cm^{-1} and 1588 cm^{-1} respectively in the Raman spectra of kerogen (Fig. 18a), while the band gap between the G and D bands is 225 cm^{-1} . According to the predecessors' proposed association between age and Raman spectral band separation [28,83,84,85], the band separation of G and D bands rises with kerogen sample maturation (Fig. 18b). The maturity of Nanpu shale kerogen (represented by vitrinite reflectance) is estimated to be around $R_o = 0.6\%$, which is comparable with the experimental R_o of 0.63% obtained from the vitrinite reflectance experiment.

4.3. CO_2 quantity adsorbed and pore size distribution (PSD) of kerogen

The CO_2 quantity adsorbed and PSD of kerogen can be obtained through CO_2 adsorption experiments. At the same time, the kerogen model we have established can also use the Grand Canonical Monte Carlo (GCMC) method in MD simulation to analyze the adsorption of

CO_2 . Comparing the CO_2 quantity adsorbed simulated by the established kerogen model with the experimental CO_2 quantity adsorbed is a very effective validation method. After verification, it was found that the CO_2 quantity adsorbed obtained from our kerogen simulation is very close to the CO_2 quantity adsorbed obtained from experiments, further confirming the reliability of our model (Fig. 19). Monte Carlo is a simulation method that obtains a solution by calculating the statistical ensemble average of random variables [86]. In a molecular simulation, it can be used to study the adsorption properties of gases in nanopores. Through the combination of Monte Carlo and molecular dynamics simulation, the adsorption and diffusion mechanism of CO_2 in minerals can be revealed at the micro-scale [87]. The details of the GCMC simulation are shown in Table 5.

To understand the differences in PSD between kerogen sample and shale, this study conducted carbon dioxide adsorption experiments on both shale and kerogen samples. CO_2 adsorption only gives the PSD for pores less than about 2 nm in diameter. Through comparison, it can be found that the pore volume of kerogen is $0.013\text{ cm}^3/\text{g}$, and that of shale samples is $0.003\text{ cm}^3/\text{g}$. In general, the trend of increasing pore volume

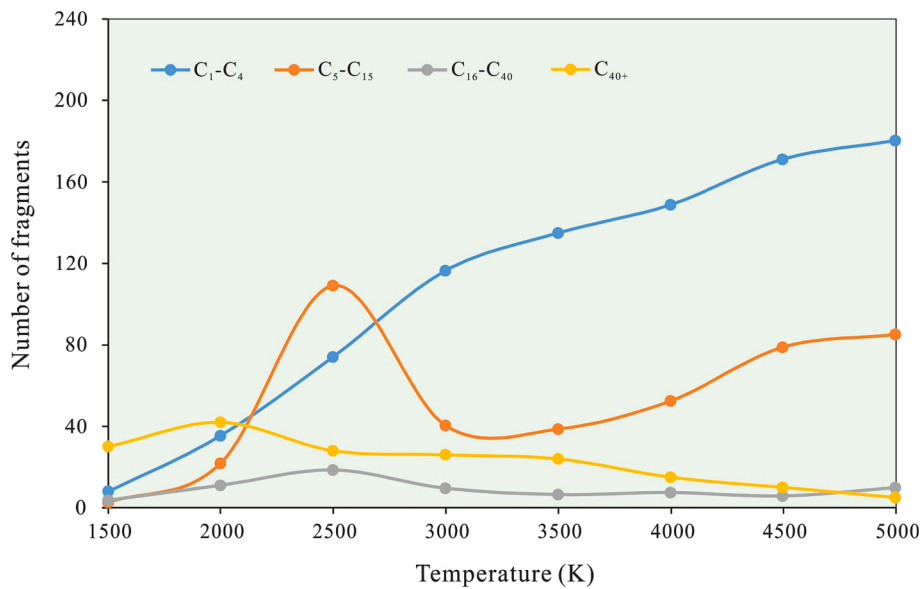


Fig. 16. Products obtained from the pyrolysis of kerogen at different temperatures.

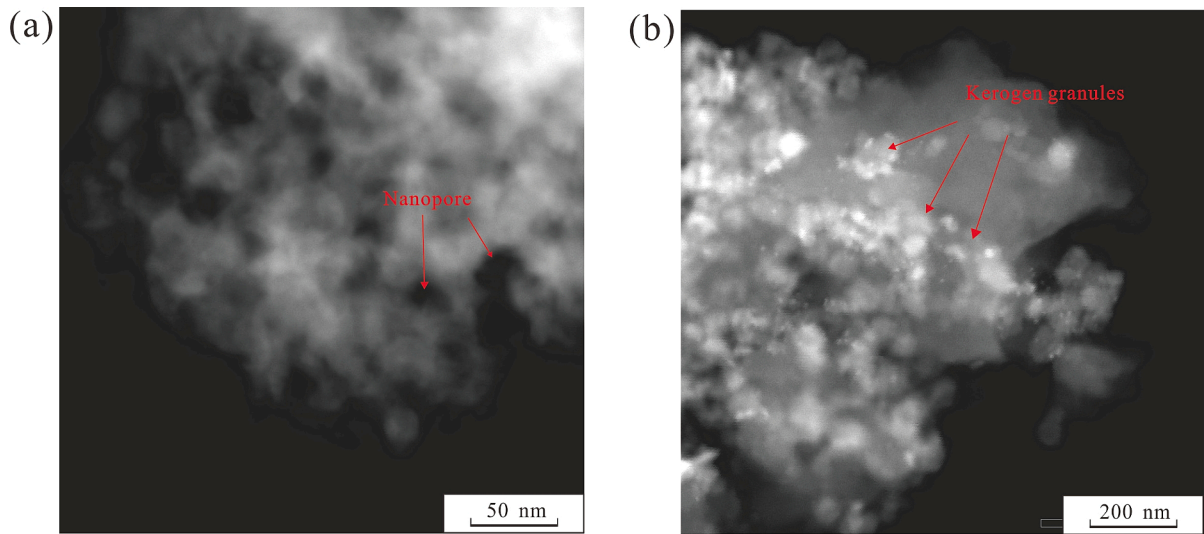


Fig. 17. STEM images of kerogen from the Nanpu shale.

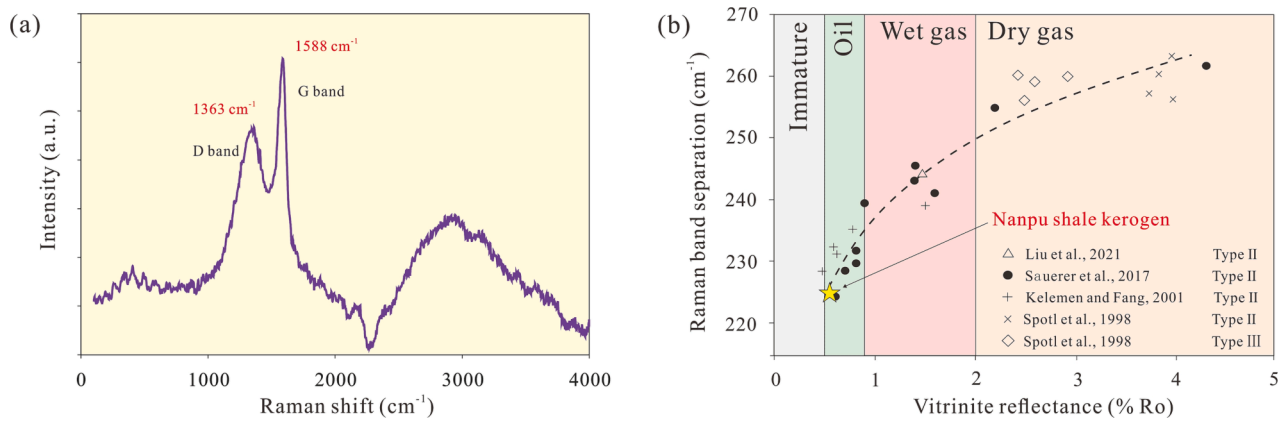


Fig. 18. Raman curve of kerogen from Nanpu shale (a) and its correlation between maturity and Raman (b) [28,83,84,85].

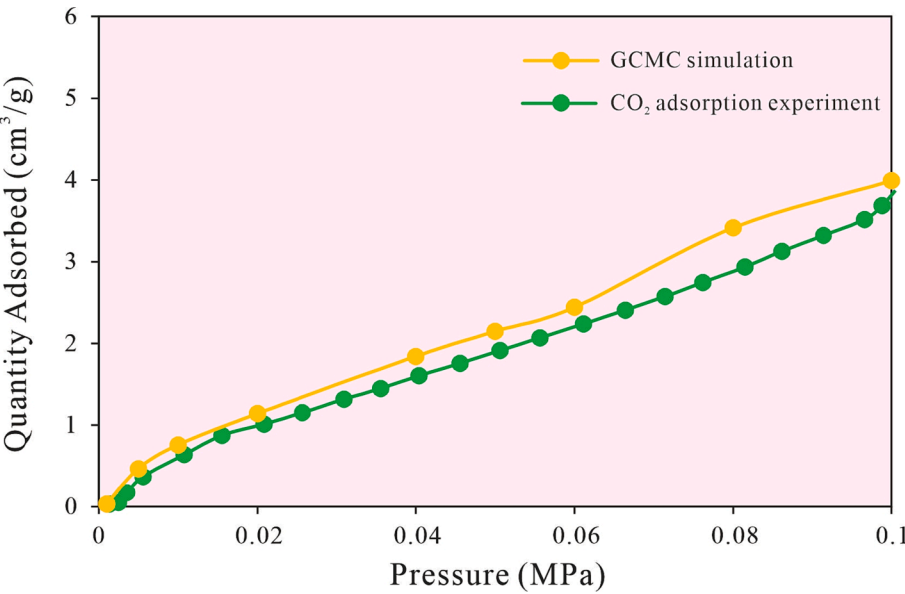


Fig. 19. Comparison between the CO₂ quantity adsorbed simulated by the kerogen model and the CO₂ quantity adsorbed obtained from experiments.

Table 5
Main input parameters of the GCMC simulation.

Simulation Modules	Parameter	Input	Unit
Sorption	Task	Fixed pressure	MPa
	Monte Carlo method	Metropolis	/
	Equilibration steps	3,000,000	step
	Production steps	5,000,000	step
	Force field	COMPASS	/
	Electrostatic Summation method	Ewald	/
	Van der Waals Summation method	Atom based	/
	Cutoff distance	15.5	Å

across all pore sizes is consistent (Fig. 20). However, the PSD of kerogen is significantly larger than that of shale samples.

5. Conclusion

The average molecular structure of the kerogen from the Nanpu shale was built in this study using elemental analysis, ¹³C NMR, XPS, FTIR, and MD simulations. The pyrolysis simulation of the kerogen was also carried out. The main understanding is as follows:

- (1) The chemical formula of the 2D molecular structure of the kerogen from the Nanpu shale was finally established to be C₁₉₉H₂₄₀O₂₀N₆S₂. The final 3D molecular structure model of kerogen is a cubic crystal cell with periodic boundary conditions built from 10 2D single molecular structures of kerogen, with a density of 1.106 g/cm³ and a box size of 3.597 nm × 3.597 nm × 3.597 nm.
- (2) The kerogen structure of the Nanpu shale is characterized by a

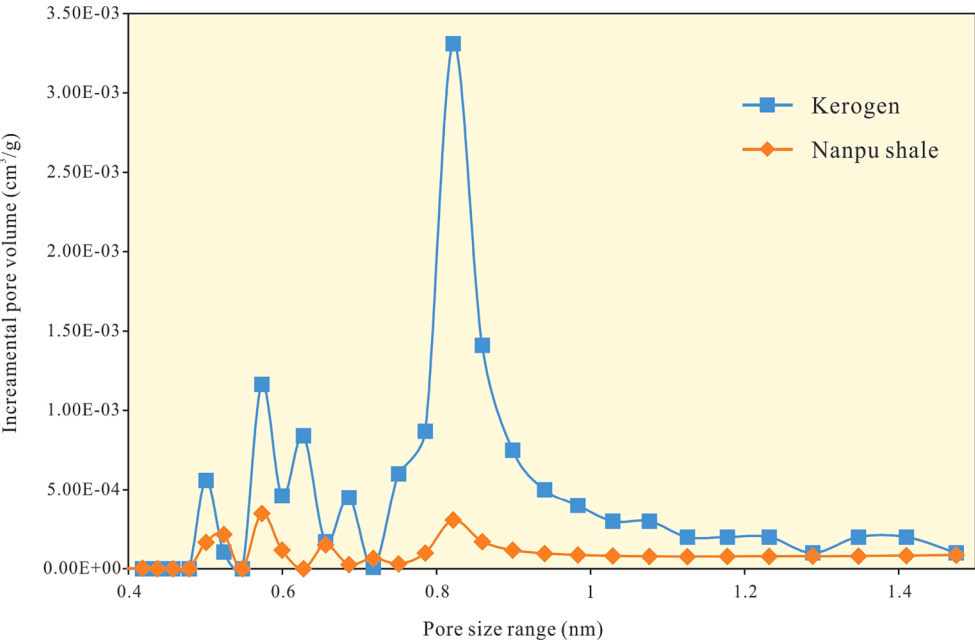


Fig. 20. Comparison of PSD between shale samples and kerogen samples obtained from CO₂ adsorption.

network structure made up primarily of aliphatic and aromatic compounds. Nitrogen is present in the kerogen as pyrrole, pyridine, and quaternary amines, while sulfur and its compounds are mainly present in the kerogen as aliphatic sulfur and thiophene.

(3) As the temperature increases (250 ps reaction time), the number of molecules produced by the pyrolysis of kerogen gradually increases. At 1500 K, the pyrolysis reaction almost did not occur. When the pyrolysis temperature of kerogen in the Nanpu shale exceeds 5000 K, the system remains basically unchanged, and the pyrolysis of kerogen is less affected by temperature. As the pyrolysis temperature increases, the amount of H₂O gradually increases, but when the temperature exceeds 2500 K, the rate of H₂ generation significantly increases. As the temperature increases, H₂O and H₂ are greatly affected by temperature, while CO₂ is less affected by temperature. Temperature is an important factor affecting the composition of pyrolysis products. The generation of liquid products (C₅–C₄₀) mainly occurs in the low-temperature region. As the temperature increases, the overall number of gaseous hydrocarbons (C₁–C₄) shows a gradually increasing trend. When the temperature exceeds 2500 K, the quantity of heavy Shale oil (C₁₆–C₄₀) begins to significantly decrease due to secondary cracking reactions.

CRediT authorship contribution statement

Kanyuan Shi: Writing – original draft, Software, Methodology, Data curation, Conceptualization, Formal analysis, Funding acquisition. **Junqing Chen:** Writing – review & editing, Visualization, Validation, Supervision, Project administration, Funding acquisition. **Xiongqi Pang:** Writing – review & editing, Resources, Project administration, Methodology, Funding acquisition. **Fujie Jiang:** Project administration, Supervision. **Shasha Hui:** Investigation, Software, Writing – review & editing. **Sijia Zhang:** Conceptualization, Software, Supervision, Validation. **Hong Pang:** Formal analysis, Validation, Visualization. **Yuying Wang:** Supervision, Validation, Visualization. **Di Chen:** Software, Supervision, Validation. **Xiaobin Yang:** Conceptualization, Data curation, Formal analysis. **Bingyao Li:** Software, Validation, Visualization. **Tingyu Pu:** Conceptualization, Software, Validation.

Declaration of Competing Interest

The authors declare that they have no known competing financial interests or personal relationships that could have appeared to influence the work reported in this paper.

Data availability

Data will be made available on request.

Acknowledgements

Thank you to the 6 reviewers for reviewing the article. Your suggestions have greatly improved the quality of the manuscript. This work was supported by the National Natural Science Foundation of China (Grant number 42102145); the Science Foundation of China University of Petroleum, Beijing (Grant number 2462022YXZZ007); the CNPC Science and Technology Major Project of the Fourteenth Five-Year Plan (Grant number 2021DJ0101), AAPG Foundation Grants-in-Aid Program (Grant number 34692939); and the Joint Fund of the National Natural Science Foundation of China (Grant number U19B6003-02-04).

Appendix A. Supplementary material

Supplementary data to this article can be found online at <https://doi.org/10.1016/j.fuel.2023.129474>.

References

- [1] Zou CN, Zhu RK, Wu ST, Yang Z, Tao SZ, Yuan XJ, et al. Types, characteristics, genesis, and prospects of conventional and unconventional hydrocarbon accumulations: taking tight oil and tight gas in China as an instance. *Acta Pet Sin* 2012;33(02):173–87. <https://doi.org/10.7623/syxb2012.02001>.
- [2] Li SQ, Liu YT, Liang X, Zhu DD. Theoretical insight into the effect of polar organic molecules on heptane-water interfacial properties using molecular dynamic simulation. *J Pet Sci Eng* 2022;212:110259. <https://doi.org/10.1016/j.petrol.2022.110259>.
- [3] Hu T, Pang XQ, Jiang FJ, Zhang CX, Wu GY, Hu ML, et al. Dynamic continuous hydrocarbon accumulation (DCHA): Existing theories and a new unified accumulation model. *Earth Sci Rev* 2022;232:104109. <https://doi.org/10.1016/j.earscirev.2022.104109>.
- [4] Wang YW, Han XX, Zheng G, Jiang XM. Thermal cracking of the large molecular alcohols in shale oil by experimental study and kinetic modeling. *J Anal Appl Pyroly* 2022;168:105749. <https://doi.org/10.1016/j.jaap.2022.105749>.
- [5] Yang S, Zhao CP, Ji BY, He YF. Adsorption isotherm calculation and mechanism of high pressure and high temperature shale gases. *Fuel* 2023;331:125854. <https://doi.org/10.1016/j.fuel.2022.125854>.
- [6] EIA, World Shale Resource Assessments, (2015).
- [7] EIA, Energy Outlook 2020, (2021). <https://www.eia.gov/outlooks/aeo/>.
- [8] Cao J, Kong LY, Guo T, Shi P, Wang C, Tu YM, et al. Molecular dynamics simulations of ion migration and adsorption on the surfaces of AFM hydrates. *Appl Surf Sci* 2023;615:156390. <https://doi.org/10.1016/j.apsusc.2023.156390>.
- [9] Wang R, Liao B, Wang JT, Sun JS, Wang YD, Wang JL, et al. Microscopic molecular insights into methane hydrate growth on the surfaces of clay minerals: Experiments and molecular dynamics simulations. *Chem Eng J* 2023;451:138757. <https://doi.org/10.1016/j.cej.2022.138757>.
- [10] Shi KY, Chen JQ, Pang XQ, Jiang FJ, Hui SS, Pang H, et al. Effect of wettability of shale on CO₂ sequestration with enhanced gas recovery in shale reservoir: Implications from molecular dynamics simulation. *J Nat Gas Sci Eng* 2022;107:104798. <https://doi.org/10.1016/j.jngse.2022.104798>.
- [11] Dehmani Y, Juliette L, Ayoub D, Lotfi S, Adrián BP, Taibi L, et al. Unravelling the adsorption mechanism of phenol on zinc oxide at various coverages via statistical physics, artificial neural network modelling and ab initio molecular dynamics. *Che Eng J* 2023;452:139171. <https://doi.org/10.1016/j.cej.2022.139171>.
- [12] Xu JL, Zhan SY, Wang WD, Su YL, Wang H. Molecular dynamics simulations of two-phase flow of n-alkanes with water in quartz nanopores. *Che Eng J* 2022;430:132800. <https://doi.org/10.1016/j.cej.2021.132800>.
- [13] Li JB, Wang M, Jiang CQ, Lu SF, Li Z. Sorption model of lacustrine shale oil: Insights from the contribution of organic matter and clay minerals. *Energy* 2022;260:125011. <https://doi.org/10.1016/j.energy.2022.125011>.
- [14] Yan LF, Chang YH, Hassanizadeh SM, Senbo X, Amir R, Carl FB, et al. A quantitative study of salinity effect on water diffusion in n-alkane phases: From pore-scale experiments to molecular dynamic simulation. *Fuel* 2022;324:124716. <https://doi.org/10.1016/j.fuel.2022.124716>.
- [15] W. Ju, L. Yan, S.B. Feng, H.G. Xin, Y. You, W.K. Ning, G.D. Yu, Brittleness assessment of the shale oil reservoir based on neural network method: A case study of the Yanchang Formation, Ordos Basin, Uncres. (2023) 54–60. <http://doi.org/10.1016/j.uncres.2022.12.003>.
- [16] Rougier V, Julien C, Benoît D, Moussa G, Joël B. Influence of the molecular weight and physical properties of a thermoplastic polymer on its dynamic wetting behavior. *Che Eng J* 2023;269:118442. <https://doi.org/10.1016/j.ces.2022.118442>.
- [17] Chen JQ, Jiang FJ, Cong Q, Pang XQ, Ma KY, Shi KY, et al. Adsorption characteristics of shale gas in organic–inorganic slit pores. *Energy* 2023;278:127788. <https://doi.org/10.1016/j.energy.2023.127788>.
- [18] Dong XH, Xu WJ, Liu RJ, Cheng ZX, Lu N, Guo WT. Insights into adsorption and diffusion behavior of shale oil in slit nanopores: A molecular dynamics simulation study. *J Mol Liq* 2022;359:119322. <https://doi.org/10.1016/j.molliq.2022.119322>.
- [19] Zhao YL, Luo MY, Liu LF. Molecular dynamics simulations of shale gas transport in rough nanopores. *J Pet Sci Eng* 2022;217:110884. <https://doi.org/10.1016/j.petrol.2022.110884>.
- [20] Shi KY, Chen JQ, Pang XQ, Jiang FJ. Wettability of different clay mineral surfaces in shale: Implications from molecular dynamics simulations. *Pet Sci* 2023;20(2):689–704. <https://doi.org/10.1016/j.petsci.2023.02.001>.
- [21] Afagwu C, Saad A, Ruud W, Mohamed M. Multiscale and multiphysics production forecasts of shale gas reservoirs: new simulation scheme based on Gaussian pressure transients. *Fuel* 2023;336:127142. <https://doi.org/10.1016/j.fuel.2022.127142>.
- [22] Yu XR, Li J, Chen ZX, Wu KL, Zhang LY, Hui G, et al. Molecular dynamics computations of brine–CO₂/CH₄–shale contact angles: implications for CO₂ sequestration and enhanced gas recovery. *Fuel* 2020;280:118590. <https://doi.org/10.1016/j.fuel.2020.118590>.
- [23] Behar F, Vandenbroucke M. Chemical Modelling of Kerogens. *Org Geochem* 1987;11(1):15–24. [https://doi.org/10.1016/0146-6380\(87\)90047-7](https://doi.org/10.1016/0146-6380(87)90047-7).
- [24] Siskin M, Scouten CG, Rose KD. Detailed Structural Characterization of the Organic Material in Rundle Ramsay Crossing and Green River Oil Shales. *Fuel* 1995;37(1):143–58. [https://doi.org/10.1016/0140-6701\(96\)86369-7](https://doi.org/10.1016/0140-6701(96)86369-7).
- [25] X. Ru, Z. Cheng, L. Song, H.Y. wang, J.F. Ling, Experimental and computational studies on the average molecular structure of Chinese Huadian oil shale kerogen, *Journal of Molecular Structure*, 1030(51) (2012) 10–18. <http://doi.org/10.1016/j.molstruc.2012.07.072>.

- [26] Wang Q, Huang ZY, Chi MS, Shi JX, Wang ZC, Sui Y. Analysis of chemical structure characteristics of oil shale kerogen. *J Chem Ind* 2015;66(05):1861–6. <https://doi.org/10.11949/j.issn.0438-1157.20141798>.
- [27] Guan XH, Liu Y, Wang D, Wang Q, Chi M, Liu S, et al. Three-Dimensional Structure of Huadian Oil Shale Kerogen Model: An Experimental and Theoretical Study. *Energy Fuels* 2015;9(7):4122–36. <https://doi.org/10.1021/ef502759q>.
- [28] Liu Y, Liu S, Zhang R, Zhang Y. The molecular model of Marcellus shale kerogen: Experimental characterization and structure reconstruction. *Int J of Coal Geol* 2021;246:246. <https://doi.org/10.1016/J.COAL.2021.103833>.
- [29] Berkowitz N. *The Chemistry of Coal*. New York: Elsevier Science Pub. Inc.; 1985.
- [30] Cantor DM. Nuclear magnetic resonance spectrometric determination of average molecular structure parameters for coal-derived liquids. *Anal Chem* 1978;50(8):1185–7. <https://doi.org/10.1021/ac50030a044>.
- [31] Dong XG, Lei QF, Feng WJ, Yu QS. Thermogravimetric analysis of petroleum asphaltenes along with estimation of average chemical structure by nuclear magnetic resonance spectroscopy. *Thermochim Acta* 2005;427(1–2):149–53. <https://doi.org/10.1016/j.tca.2004.09.004>.
- [32] Li X, Zheng M, Ren C, Guo L. ReaxFF molecular dynamics simulations of thermal reactivity of various fuels in pyrolysis and combustion. *Energy Fuels* 2021;35(15):11707–39. <https://doi.org/10.1021/acs.energyfuels.1c01266>.
- [33] Chen Z, Pei J, Li R, Xiao F. Performance characteristics of asphalt materials based on molecular dynamics simulation—A review. *Constr Build Mater* 2018;189:695–710. <https://doi.org/10.1016/j.conbuildmat.2018.09.038>.
- [34] Rajabpour S, Mao Q, Nayir N, Robinson JA, van Duin ACT. Development and applications of ReaxFF reactive force fields for group-III gas-phase precursors and surface reactions with graphene in metal–organic chemical vapor deposition synthesis. *J Phys Chem C* 2021;125(19):10747–58. <https://doi.org/10.1021/acs.jpcc.1c01965>.
- [35] Li GX, Zhang FJ, Huang QF, Wang JJ, Niu B, Zhang YY, et al. Molecular insight into pyrolysis processes via reactive force field molecular dynamics: A state-of-the-art review. *J Anal Appl Pyrol* 2022;166:105620. <https://doi.org/10.1016/j.jaap.2022.105620>.
- [36] Liu J, Li X, Guo L, Zheng M, Han JY, Yuan XL, et al. Reaction analysis and visualization of ReaxFF molecular dynamics simulations. *J Mol Graph* 2014;53:13–22. <https://doi.org/10.1016/j.jmgraph.2014.07.002>.
- [37] Salmon E, Duin V, Adri CT, Lorant F, Marquaire PM, Goddard WA. Thermal decomposition process in algaeana of *Botryococcus braunii* race L. Part 2: Molecular dynamics simulations using the ReaxFF reactive force field. *Org Geochem* 2009;40(3):400–15. <https://doi.org/10.1016/j.orggeochem.2008.08.012>.
- [38] Zhang JH, Wu R, Liu X, Gao SQ, Xu GW. Preliminary understanding of initial reaction process for subbituminous coal pyrolysis with molecular dynamics simulation. *Fuel* 2014;134. <https://doi.org/10.1016/j.fuel.2014.06.005>.
- [39] Li W, Zhu YM, Wang GF, Wang Y, Liu Y. Molecular model and ReaxFF molecular dynamics simulation of coal vitrinite pyrolysis. *J Mol Model* 2015;21(8):188. <https://doi.org/10.1007/s00894-015-2738-6>.
- [40] Hong D, Guo X. Molecular dynamics simulations of Zhundong coal pyrolysis using reactive force field. *Fuel* 2017;210:58–66. <https://doi.org/10.1016/j.fuel.2017.08.061>.
- [41] Chen D, Pang XQ, Li L, Jiang FJ, Liu GY, Li M, et al. Organic geochemical characteristics and shale oil potential of the middle Eocene early-mature shale in the Nanpu Sag, Bohai Bay Basin, Eastern China. *Mar Pet Geol* 2021;133:105248. <https://doi.org/10.1016/j.marpetgeo.2021.105248>.
- [42] Saxby JD. Isolation of kerogen in sediments by chemical methods. *Chem Geol* 1970;6:173–84. [https://doi.org/10.1016/0009-2541\(70\)90017-3](https://doi.org/10.1016/0009-2541(70)90017-3).
- [43] Pang XQ, Li M, Li BY, Wang T, Hui SS, Liu Y, et al. Main controlling factors and movability evaluation of continental shale oil. *Earth Sci Rev* 2023;243:104472. <https://doi.org/10.1016/j.earscirev.2023.104472>.
- [44] Wang Q, Wang XM, Pan S. The three-dimensional molecular structure model of Fushun oil shale kerogen, China. *J Mol Struct* 2022;1255:132380. <https://doi.org/10.1016/j.molstruc.2022b.132380>.
- [45] Marzec A. Towards an Understanding of the Coal Structure: A Review. *Fuel Process Technol* 2002;77–78:25–32. [https://doi.org/10.1016/S0378-3820\(02\)00045-0](https://doi.org/10.1016/S0378-3820(02)00045-0).
- [46] Ding DS, Liu GJ, Fu B. Influence of Carbon Type on Carbon Isotopic Composition of Coal from the Perspective of Solid-state ^{13}C NMR. *Fuel* 2019;245:174–80. <https://doi.org/10.1016/j.fuel.2019.02.072>.
- [47] Chu W, Cao XY, Schmidt-Rohr K, Birdwell JE, Mao JD. Investigation into the Effect of Heteroatom Content on Kerogen Structure Using Advanced ^{13}C Solid-State Nuclear Magnetic Resonance Spectroscopy. *Energy Fuels* 2019;33(2):645–53. <https://doi.org/10.1021/acs.energyfuels.8b01909>.
- [48] Huang L, Ning Z, Wang Q, Qi Rongrong J, Li Y, Zeng HT, et al. Thermodynamic and Structural Characterization of Bulk Organic Matter in Chinese Silurian Shale: Experimental and Molecular Modeling Studies. *Energy Fuels* 2017;31(5). <https://doi.org/10.1021/acs.energyfuels.7b00132>.
- [49] Lee H, Arash A, Liu B, Mohammadreza S. Mehdi Ostadhasan, Molecular weight variations of kerogen during maturation with MALDI-TOF-MS. *Fuel* 2020;269:117452. <https://doi.org/10.1016/j.fuel.2020.117452>.
- [50] Wang Q, Ye JB, Yang HY. Chemical composition and structural characteristics of oil shales and their kerogens using FTIR and solid-state ^{13}C NMR. *Energy Fuels* 2016;30(8):6271–80. <https://doi.org/10.1021/acs.energyfuels.6b00770>.
- [51] Kozłowski M. XPS study of reductively and non-reductively modified coals. *Fuel* 2004;83(3):259–65. <https://doi.org/10.1016/j.fuel.2003.08.004>.
- [52] Hui SS, Pang XQ, Chen ZH, Hu T, Shi KY, Di GD, et al. Quantifying the relative contribution and evolution of pore types to shale reservoir space: Constraints from over-mature marine shale in the Sichuan Basin, SW China. *J Asian Earth Sci* 2023;105625. <https://doi.org/10.1016/j.jseas.2023.105625>.
- [53] Thommes M, Kaneko K, Neimark AV, Olivier JP, Rodríguez-Reinoso F, Rouquerol J, et al. Physisorption of gases, with special reference to the evaluation of surface area and pore size distribution (IUPAC Technical Report). *Pure Appl Chem* 2015;87(9–10):1051–69. <https://doi.org/10.1515/pac-2014-1117>.
- [54] Lowell S, Shields JE, Thomas MA, Thommes M. *Characterization of Porous Solids and Powders: Surface Area, Pore Size and Density*. Dordrecht: Springer, Netherlands; 2004.
- [55] Xiang J, Liu JW, Xu J, Su S, Tang H, Hu Y, et al. The fluorescence interference in Raman spectrum of raw coals and its application for evaluating coal property and combustion characteristics. *Proc Combust Inst* 2019;37(3):3053–60. <https://doi.org/10.1016/j.proci.2018.06.172>.
- [56] Knaack DR, Leybourne MI, Layton-Matthews D, McDonald AM, Vuletich A, Chipley D, et al. Manganese nodules NOD-A-1 and NOD-P-1: Implications of pre-treatment on oxygen isotopes and mineralogy. *Chem Geol* 2020;558:119924. <https://doi.org/10.1016/j.chemgeo.2020.119924>.
- [57] Dong H, Wang ZH, Dong M, Li H, Wei XY, Liang JW. Application of Laser Raman spectroscopy in the study of organic inclusions: A case study on oil and gas inclusions in the 8th member of the shihezi formation in western sulige gasfield. *Journal of Geomechanics* 2017;23(4):594–601. in Chinese.
- [58] Qian BB, Liu C, Jian MP, Hu XI, Zhou S. Synthesis of in-situ Al_3^{+} -defected iron oxide nanoflakes from coal ash: A detailed study on the structure, evolution mechanism and application to water remediation. *J. Hazard. Mater.* 2020;395:122696. <https://doi.org/10.1016/j.jhazmat.2020.122696>.
- [59] Goldenberg M, Vreeman G, Sun DJ, Moffitt M, Li M, Zernik M, et al. A material-sparing simplified buoyancy method for determining the true density of solids. *Int J Pharm* 2023;635:122694. <https://doi.org/10.1016/j.ijpharm.2023.122694>.
- [60] Elsergany RN, Vreeman G, Sun CQC. An approach for predicting the true density of powders based on in-die compression data. *Int J Pharm* 2023;637:122875. <https://doi.org/10.1016/j.ijpharm.2023.122875>.
- [61] Liu SH, Wei LH, Zhou Q, Yang TH, Li SB, Zhou Q. Simulation strategies for ReaxFF molecular dynamics in coal pyrolysis applications: A review. *J Anal Appl Pyrol* 2023;170. <https://doi.org/10.1016/J.JAAP.2023.105882>.
- [62] Tong J, Han X, Wang S, Jiang XM. Evaluation of Structural Characteristics of Huadian Oil Shale Kerogen Using Direct Techniques (Solid-State ^{13}C NMR, XPS, FT-IR, and XRD). *Energy & Fuels: An American Chemical Society Journal* 2011;25:4006–13. <https://doi.org/10.1021/ef200738p>.
- [63] Ungerer P, Colléll J, Yiannourakou M. Molecular modeling of the volumetric and thermodynamic properties of kerogen: Influence of organic type and maturity. *Energy Fuels* 2015;29(1):91–105. <https://doi.org/10.1021/ef502154k>.
- [64] Yang F, Hou Y, Wu W, Muge N, Ren SH, Wang Q. A new insight into the structure of Huolinhe lignite based on the yields of benzene carboxylic acids. *Fuel* 2017;189. <https://doi.org/10.1016/j.fuel.2016.10.112>.
- [65] Painter PC, Snyder RW, Starsinic M, Coleman MM, Kuehn DW, Davis A. Concerning the Application of FT-IR to the Study of coal: a critical Assessment of Band Assignments and the Application of Spectral Analysis Programs. *Appl Spectrosc* 1981;35(5):475–85. <https://doi.org/10.1366/0003702814732256>.
- [66] Vandegrift GF, Winans RE, Scott RG, Scott RG, Horwitz EP. Quantitative study of the carboxylic acids in Green River oil shale bitumen. *Fuel* 1980;59(9). [https://doi.org/10.1016/0016-2361\(80\)90124-6](https://doi.org/10.1016/0016-2361(80)90124-6).
- [67] Ibrahimov RA, Bissada KA. Comparative Analysis and Geological Significance of Kerogen Isolated Using Open-System (Palynological) Versus Chemically and Volumetrically Conservative sed-System Methods. *Org Geochem* 2010;41(8):800–11. <https://doi.org/10.1016/j.orggeochem.2010.05.006>.
- [68] Colléll J, Ungerer P, Galliero G, Yiannourakou M, Montel F, Pujol M. Molecular Simulation of Bulk Organic Matter in Type II Shales in the Middle of the Oil Formation Window. *Energy Fuels* 2014;28. <https://doi.org/10.1021/ef5021632>.
- [69] Wang Q, Liu Q, Wang ZC. Characterization of organic nitrogen and sulfur in the oil shale kerogens. *Fuel Process Technol* 2017;160:170–7. <https://doi.org/10.1016/j.fuproc.2017.02.031>.
- [70] Zhou ZJ, Guo LZ, Chen LP. Study of Pyrolysis of Brown Coal and Gasification of Coal-water Slurry using the ReaxFF Reactive Force Field. *Int J Energy Res* 2018;42:2465–80. <https://doi.org/10.1002/er.4029>.
- [71] Guo L, Zhou Z, Chen LP, Shan SQ, Wang ZH. Study of the pyrolysis of coals of different rank using the ReaxFF reactive force field. *J Mol Model* 2019;25(6). <https://doi.org/10.1007/s00894-019-4044-1>.
- [72] Zheng M, Li X, Bai J, Guo L. Chemical structure effects on coal pyrolyzates and reactions by using large-scale reactive molecular dynamics. *Fuel* 2022;327:125089. <https://doi.org/10.1016/J.FUEL.2022.125089>.
- [73] Wang QD, Wang JB, Li JQ, Tan NX, Li XY. Reactive molecular dynamics simulation and chemical kinetic modeling of pyrolysis and combustion of n-dodecane. *Combust Flame* 2011;158(2):217–26. <https://doi.org/10.1016/j.combustflame.2010.08.010>.
- [74] Zheng M, Li XX, Liu J, Wang Z, Gong XM, Guo L, et al. Pyrolysis of Liulin Coal Simulated by GPU-Based ReaxFF MD with Cheminformatics Analysis. *Energy Fuels* 2014;28(1):522–34. <https://doi.org/10.1021/ef402140n>.
- [75] Qian YN, Zhan JH, Lai DG, Li MY, Liu XX, Xu GW. Primary understanding of non-isothermal pyrolysis behavior for oil shale kerogen using reactive molecular dynamics simulation. *Int J Hydrog Energy* 2016;41(28):12093–100. <https://doi.org/10.1016/j.ijhydene.2016.05.106>.
- [76] Huang ZK, Liang T, Zhan ZW, Zou YR, Li MW, Peng PA. Chemical structure evolution of kerogen during oil generation. *Mar Pet Geol* 2018;98:422–36. <https://doi.org/10.1016/j.marpetgeo.2018.08.039>.
- [77] Liang T, Zou YR, Zhan ZW, Lin XH, Shi J, Peng PA. An evaluation of kerogen molecular structures during artificial maturation. *Fuel* 2020;265:116979. <https://doi.org/10.1016/j.fuel.2019.116979>.

- [78] Cao HR, Lei Y, Wang XY, Zou YR, Peng PA. Molecular structure evolution of Type I kerogen during pyrolysis: Case study from the Songliao Basin, NE China. *Mar Pet Geol* 2021;134:105338. <https://doi.org/10.1016/j.marpetgeo.2021.105338>.
- [79] Xu JZ, Chen ZX, Zhou DS, Nie WC, Li R. Review on the characteristics of pyrolysis during in-situ conversion of oil shale. *Journal of Southwest Petroleum University (Science & Technology Edition)* 2021;43(5):220–6. in Chinese.
- [80] Behar F, Kressmann S, Rudkiewicz JL, Vandenbroucke M. Experimental simulation in a confined system and kinetic modelling of kerogen and oil cracking. *Org Geochem* 1992;19(1–3):173–89. [https://doi.org/10.1016/0146-6380\(92\)90035-V](https://doi.org/10.1016/0146-6380(92)90035-V).
- [81] Alhesan JSA, Fei Y, Marshall M, Jackson WR, Qi Y, Chaffee AL, et al. Long time, low temperature pyrolysis of El-Lajjun oil shale. *J Anal Appl Pyrol* 2018;130:135–41. <https://doi.org/10.1016/j.jaap.2018.01.017>.
- [82] Dai JX, Zou CN, Liao SM, Dong DZ, Ni YY, Huang JL, et al. Geochemistry of the extremely high thermal maturity Longmaxi shale gas, southern Sichuan Basin. *Org Geochem* 2014;74:3–12. <https://doi.org/10.1016/j.orggeochem.2014.01.018>.
- [83] Spötl C, Houseknecht DW, Jaques RC. Kerogen maturation and incipient graphitization of hydrocarbon source rocks in the Arkoma Basin, Oklahoma and Arkansas: a combined petrographic and Raman spectrometric study. *Org Geochem* 1998;28(9–10):535–42. [https://doi.org/10.1016/S0146-6380\(98\)00021-7](https://doi.org/10.1016/S0146-6380(98)00021-7).
- [84] Kelemen SR, Fang HL. Maturity trends in Raman spectra from kerogen and coal. *Energy Fuel* 2001;15. <https://doi.org/10.1021/ef402140n>.
- [85] Sauerer B, Craddock PR, Aljohani MD, Alsamadony KL, Abdallah W. Fast and accurate shale maturity determination by Raman spectroscopy measurement with minimal sample preparation. *Int J Coal Geol* 2017;173:150–7. <https://doi.org/10.1016/j.coal.2017.02.008>.
- [86] Kadoura A, Narayanan Nair AK, Sun SY. Adsorption of carbon dioxide, methane, and their mixture by montmorillonite in the presence of water. *Microporous Mesoporous Mater* 2016;225:331–41. <https://doi.org/10.1016/j.micromeso.2016.01.010>.
- [87] Li CQ, Liu SQ, Tian HQ, Liang JX, Li YB. Molecular simulation of adsorption and diffusion behavior of CO₂ in pyrophyllite. *Fuel* 2023;321:128917. <https://doi.org/10.1016/j.fuel.2023.128917>.